

An improved OMI ozone profile research product version 2.0 with collection 4 L1b data and algorithm updates

Juseon Bak^{1,*}, Xiong Liu², Yang Kai³, Gonzalo Gonzalez Abad²,

Ewan O`Sullivan², Kelly Chance², Cheol-Hee Kim^{1,4}

¹Institute of Environmental Studies, Pusan National University, Busan 46241, Republic of Korea

²Smithsonian Astrophysical Observatory (SAO), Center for Astrophysics | Harvard & Smithsonian, Cambridge, MA 02138, USA

³Department of Atmospheric Sciences, University of Maryland, College Park, MD 20742, USA.

⁴Department of Atmospheric Sciences, Pusan National University, Busan 46241, South Korea

*Corresponding Author Juseon Bak (juseonbak@pusan.ac.kr) & Xiong Liu (xliu@cfa.harvard.edu)

Abstract

We describe the new and improved version ~~2 (V2)~~ of the ozone profile research product from the Ozone Monitoring Instrument (OMI) on the Aura satellite. One of the major changes is to switch the OMI L1b data from collection 3 to the recent collection 4 as well as the accompanying auxiliary datasets. The algorithm details are updated on radiative transfer (~~RT~~) model calculation and measurement calibrations, along with the input changes of meteorological data, and with the use of a tropopause-based ozone profile climatology, an improved high-resolution solar reference spectrum, and a recent ozone absorption cross-section dataset. A super Gaussian is applied to better represent OMI slit functions, instead of a normal Gaussian. The effect of slit function errors on the spectral residuals is further accounted for as pseudo absorbers in the iterative fit process. The OMI irradiances are averaged into monthly composites to reduce noise uncertainties in OMI daily measurements and to cancel out the temporal variations of instrument characteristics that are common -in both ~~the common degradation of~~ radiance and irradiance measurements which was previously neglected due to use of climatological composites. The empirical soft calibration spectra are re-derived to be consistent with the updated implementations and derived annually to remove the ~~timely varying-dependent~~ systematic biases between measured and simulated radiances. The “common mode” correction spectra are derived from remaining residual spectra after soft calibration as a function of solar zenith angle. The common mode is included as a pseudo absorber in the iterative fit process, which helps to reduce the discrepancies of ozone retrieval accuracy between lower and higher solar zenith angles and between nadir and off-nadir pixels. Validation with ozonesonde measurements demonstrates the improvements of ozone profile retrievals in the troposphere, especially around the tropopause. The retrieval quality of tropospheric column ozone is improved with respect to the seasonal consistency between winter and summer as well as the long-term consistency before and after the row-anomaly occurrence.

1. Introduction

The Smithsonian Astrophysical Observatory (SAO) ozone profile algorithm was originally developed to retrieve ozone profiles with sensitivity down to the lower troposphere from Global Ozone Monitoring Experiment (GOME) measurements (Liu et al., 2005) and has been continuously adapted to Ozone Monitoring Instrument (OMI) (Liu et al., 2010), GOME/2A (Cai et al., 2012), Ozone Mapping and Profiler Suite (OMPS) (Bak et al., 2017), TROPospheric Monitoring Instrument (TROPOMI) (Zhao et al., 2021), Geostationary Environment Monitoring Spectrometer (GEMS) (Bak et al., 2019a), and Tropospheric Emissions: Monitoring of Pollution (TEMPO) (Zoogman et al., 2017). The SAO algorithm has been put into production in the NASA's OMI Science Investigator-led Processing System (SIPS) to create the OMI ozone profile research product titled OMPROFOZ v0.93 (referred to as v1, hereafter) that is publically distributed via the Aura Validation Data Center (AVDC) (<https://avdc.gsfc.nasa.gov/pub/data/satellite/Aura/OMI/V03/L2/OMPROFOZ/>). The OMPROFOZ product has ~~been~~ contributed to a better understanding of chemical and dynamical ozone variability associated with anthropogenic pollution over central and eastern China (Hayashida et al., 2015; Wei et al., 2022), transport of anthropogenic pollution in free troposphere (Walker et al., 2010) and stratospheric ozone intrusion (Kuang et al., 2017) as well as ozone concentration changes in the Asian summer monsoon (Lu et al., 2018; Luo et al., 2018). ~~Furthermore~~Moreover, this product has been used to quantify the global tropospheric budget of ozone and to evaluate how well current chemistry-climate models reproduce the observations (Hu et al., 2017; Zhang et al., 2010). In this manner, the OMPROFZ product has provided invaluable insights. ~~OMI instrument show progressively low optical degradation over the mission, with a change of ~ 3 % in the radiance over roughly 1.5 decades (Kleipool et al., 2022). However, the long-term reliability of the OMPROFOZ product, However, its long term reliability, particularly concerning tropospheric ozone measurements, remains susceptible to optical instrument degradation. Compared to other similar space borne UV instruments, in spite that OMI has maintained much better long term stability over throughout the mission, with low optical degradation (1-2 % in radiance, 3-8 % in irradiance) and high wavelength stability (0.005-0.020 nm), compared to other similar space borne UV instruments (REF). In addition degradation (Gaudel et al., 2018; Huang et al., 2018, 2017).~~ but there has been concern over the OMI row anomaly effects appearing in 2007, becoming serious in early 2009, and currently damaging about half of the instrument's viewing capability (Schenkeveld et al., 2017). So far, satellite ozone profile products have not been reliable for long term analysis, especially for the tropospheric ozone measurements due to their susceptibility to the optical degradation of instruments (Gaudel et al., 2018). Ten-years of the OMPROFOZ product were assessed in-depth in Huang et al. (2018;2017) through the spatiotemporal validation using global

72 reference dataset collected from [in-situ balloon-borne ozonesondes](#) and space-borne Microwave Limb
73 Sounder (MLS), [which is one of the payloads onboard the Aura satellite, along with the OMI instrument.](#)
74 ~~measurements.~~ They concluded noticeable discrepancies in time-series of data quality ~~due to the~~
75 ~~occurrence of serious row anomaly and suggested the need to address the spatiotemporal variations of~~
76 ~~the retrieval performance and the related cross-track dependency, and the dependence of retrieval~~
77 ~~quality on the latitude/season/viewing geometries.~~ Since the first release of OMPROFOZ data,
78 implementation details have been externally refined to improve the retrieval quality. Bak et al., (2013)
79 demonstrated improvements of ozone profile retrievals around the extratropical tropopause ~~region area~~
80 by better constraining climatological a priori information. To better represent an instrument spectral
81 response function (ISRF), Sun et al. (2017) employed a Super Gaussian function which can represent
82 more complex shapes compared to a classical Gaussian function. The slit function linearization was
83 experimented in Bak et al. (2019b) to account for the effects of errors in slit function parameters on the
84 spectral fit residuals. Moreover, the best spectroscopic inputs were investigated with respect to the
85 ozone cross-section (Bak et al., 2020; Liu et al., 2013) and the high-resolution solar reference spectrum
86 (Bak et al., 2022). To accelerate the time-consuming radiative transfer (~~RT~~) calculation, a principal
87 component analysis (PCA)-based ~~RT radiative transfer (RT)~~ model was employed as a forward model
88 with the correction scheme of RT approximation errors using look-up tables (LUTs) (Bak et al., 2021).
89 The updates to radiometric corrections were made with the time-dependent soft calibration and solar
90 zenith angle dependent common mode correction, improving the spatiotemporal consistency of retrieval
91 quality, which are detailed in this paper. Individual refinements mentioned above are incorporated in
92 the OMPROFOZ ~~version V2~~ (~~v2~~) algorithm, along with the switch of OMI L1b data product from
93 collection 3 to collection 4. Note that OMI measurements have been reprocessed to deliver the ~~new~~
94 ~~recent~~ collection 4 dataset which supersedes and improves the collection 3 with respect to the ongoing
95 instrument effects and optical degradations, drifts in electronic gain, and pixel quality flagging-
96 (Kleipool et al., 2022).

97 In this paper we describe updates made in the OMI ozone profile algorithm, discuss their impact on
98 spectral fit and ozone profile retrievals, and provide an initial quantitative assessment of tropospheric
99 ozone columns with respect to their long-term consistency. Section 2 describes OMI L1b and auxiliary
100 products used in retrieving ozone profiles, along with the retrieval methodology and OMPROFOZ v2
101 product. In section 3 the updates of implementation details are specified and verified. Section 4 presents
102 the validation results using ozonesonde measurements. This paper is summarized and concluded in
103 Section 5.

104 [2.](#)

3.2. Description of the SAO OMI ozone profile algorithm and OMPROFOZ product

2.1 OMI products

Table 1 lists the OMI standard or auxiliary products used in reprocessing OMI ozone profiles, which are publicly available through NASA's Goddard Earth Sciences Data and Information Services Center (GES DISC). OMI is a nadir-viewing UV and visible spectrometer in which two-dimensional (spectral \times spatial) charged-coupled device (CCD) detectors are employed. The collection 4 L0-1B processor was newly built based on the TROPOMI L0-1B processor at the OMI SIPS, which produces radiometrically calibrated and geolocated solar irradiances and earthshine radiances from the raw sensor measurements. Insights learned from the usage of OMI collection 3 data over the past 17 years are leveraged to correct optical and electronic aging and improve pixel quality flagging. The details of ~~updates and improvements~~switching from collection 3 to collection 4 can be found in Kleipool et al. (2022). The OML1BIRR (~~10.5067/Aura/OMI/DA1401~~) provides the daily averaged irradiance measurements. The OML1BRUG (~~10.5067/AURA/OMI/DA1402~~) contains Earth view spectral radiances taken in the global mode from the UV detector. To increase a signal to noise ratio (SNR) at shorter UV wavelengths, a measured spectrum is divided into two sub channels at ~ 310 nm and then the spatial resolution of the shorter ~~spectra~~wavelength is degraded by a factor of 2 in cross-track pixels, resulting into 48 km and 24 km at nadir ~~for 159 channels~~ in the Band 1 (UV-1, 159 channels in 264-311 nm) and ~~for 557 channels~~ in the Band 2 (UV-2, 557 channels in 307-383 nm), respectively. The spatial resolution is 13 km in the flight direction. Cloud information is taken from OMCLDO2 based on the spectral fitting of O₂-O₂ absorption band at 477 nm, while a climatological surface albedo is taken from OMLER. The OMUANC is a new ancillary product, geo-located to UV2 spatial pixels, developed ~~for to~~supporting the production of ~~the~~ OMI L2 data products in the frame of collection 4. This product contains flags to identify snow-ice pixels based on the Near real-time Ice and Snow Extent (NISE) data and to screen out anomaly rows based on the NASA flagging scheme. We use OMUANC data for taking snow-ice flags and row anomaly flags. The row anomaly (RA) is an anomaly which affects OMI measurements at all wavelengths for some particular rows of the CCD detector.

~~the quality of the level 1B radiance data at all wavelengths for specific viewing angles.~~ Only two of OMI's 60 rows in the UV2 image were initially affected in 2007, but the anomalies have become more serious since January 2009 ($\sim 30\%$), spreading to $\sim 50\%$ (rows 25-55) during the period of 2010-2012. There is no reliable correction scheme for ~~the RA row anomaly~~-affected measurements and therefore

139 flagging the row anomalies as bad data is ~~important-crucial~~ to ~~assure-ensure~~ the L2 product quality. A
140 ~~Row anomaly~~RA flags ~~are-is~~ available from both OML1BRUG and OMUANC; ~~the-The~~ former ~~relies~~
141 ~~on the is based on~~ analysis of features observed in ~~the~~ radiance measurements to identify the row
142 anomaly ~~contained-contaminated~~ pixels, referred as to the KNMI ~~flagging method~~flag, which. ~~Note that~~
143 ~~the KNMI flagging method~~ remains unchanged from collection 3 to 4 (AURA-OMI-KNMI-L01B-
144 0005-SD, 2021). ~~The NASA flag for t~~The latter is based on a statistical analysis of errors detected in
145 the ~~NASA OMI TOMS-like total column ozone data~~OMT03-L2 total column ozone, referred as to the
146 ~~NASA flagging method~~. According to Schenkeveld et al. (2017) who compared the KNMI and NASA
147 flagging results in the UV2 channel, two methods produce consistent flagging results over the full
148 course of the OMI mission, but the NASA method is likely to be stricter and ~~more~~ reliable. In this paper,
149 row anomalies are filtered out when either OML1BRUG (~~UV2 only~~) or OMUANC flags are
150 ~~raised~~flagged. The OMUFPMET and OMUFPSLV supply meteorological fields at OMI overpass
151 positions, which is further detailed in Section 3.2 where the updates to meteorological inputs in
152 OMPROFOZ are verified. ~~In-addition,We~~ ~~applied~~ OMI total column ozone product
153 (~~OMT03GOMT03d~~) to adjust the ozone profile shape used as an input for ~~is used in~~ deriving empirical
154 correction spectra (Sect. 3.8).

155

156 **Table 1 Input list of OMI data.**

Product name	Processing level (spatial resolution/band *)	Collection number	Primary variables
OML1BIRR	L1B (UV1,UV2)	4	solar irradiance
OML1BRUG	L1B (UV1, UV2)	4	Earthshine-earthshine radiance, row anomaly flag (UV2 only)
OMCLDO2	L2 (UV2)	3	cloud fraction, cloud pressure
OMUANC	L2 (UV2)	4	Row-row anomaly flag, snow ice flag
OMUFPMET	L2 (UV2)	4	Pressure-pressure profile, temperature profile
OMUFPSLV	L2 (UV2)	4	Surface-surface pressure, surface skin temperature, Thermal tropopause pressure
OMLER	L3 (0.5° x 0.5°)	3	Monthly-monthly and yearly climatology of the Earth's surface Lambert Equivalent Reflectance (LER)
OMT03d	L3 (0.25° x 0.25°)	3	Total column ozone

157 * UV1, UV2, VIS represent bands and their corresponding spatial resolutions (except for OML1BIRR) 13 x 48
158 km², 13 x 24 km², and 13 x 24 km² at nadir, respectively.

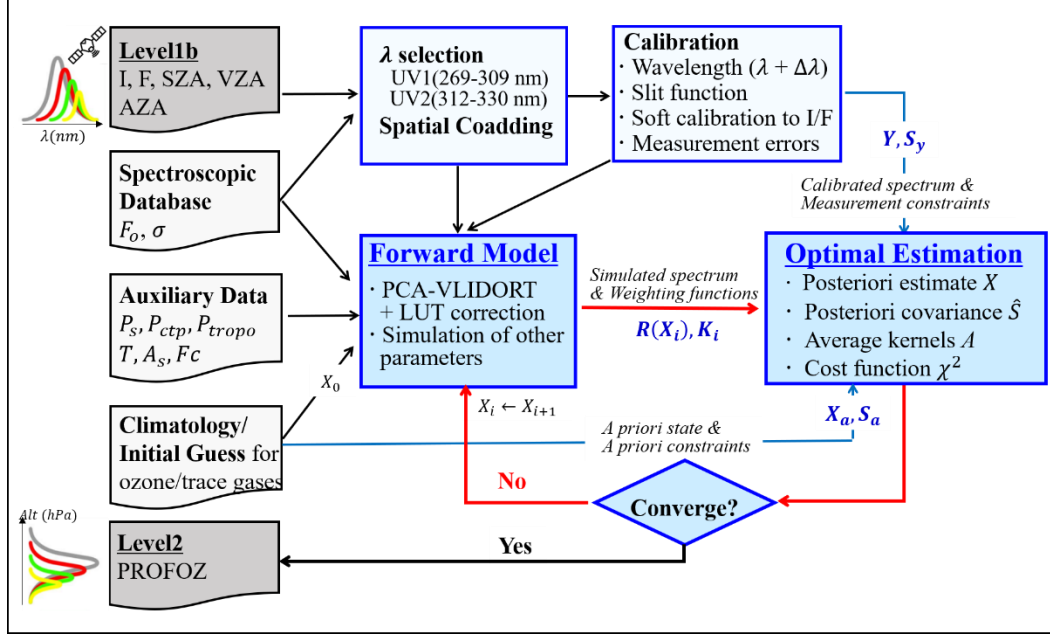
159

160

2.1.2 OMPROFOZ algorithm

As depicted in Figure 1, our algorithm is composed of an optimal estimation (OE) based inversion (Rodgers, 2000), radiative transfer (forward) model simulations, and state-of-the-art calibrations. We have ~~In our algorithm, two spectral windows: one spanning 270-309 nm in the UV-1 band and another spanning 312-330 nm in the UV-2 band are selected for 270-309 nm in the UV-1 band and 312-330 nm in the UV-2 band and.~~ Two UV-2 spatial pixels are co-added to match UV-1 spatial resolution in the cross-track direction. To meet the computational budget ~~in the previous data processing~~, OMI measurements were spatially coadded in the flight direction, reducing the spatial resolution to $48 \times 52 \text{ km}^2$ in the earlier data processing in the v1 product. In the new v2 data processing, OMPROFOZ will be released at ~~38-48~~ $\times 26 \text{ km}^2$, owing to the speed up of radiative transfer calculations described in Section 3.7. ~~The SAO ozone profile algorithm is composed of an optimal estimation (OE) based inversion (Rodgers, 2000), radiative transfer (forward) model simulations, and state of the art calibrations (Figure 1).~~

In the calibration process, a cross-correlation technique is implemented to characterize in-orbit slit functions and wavelength shift errors ($\Delta\lambda$) using a well calibrated, high resolution solar reference spectrum. ~~The wavelength drifts of OMI instrument were has shown high wavelength stability (-0.015 nm in UV-1 and 0.005 nm in UV-2 $0.005-0.020 \text{ nm}$) over the mission lifetime by (Bak et al., 2019b; Schenkeveld et al., 2017; Sun et al., 2017) and thereby additional wavelength correction is not carried out for each radiance and irradiance spectrum.~~ The empirical correction so-called soft calibration is applied for eliminating the systematic measurement biases in the wavelength range of 270 - 330 nm for ozone fitting and around 347 nm for the initial surface albedo/cloud fitting. This correction was previously applied dependent on wavelength and cross-track position, but currently updated to enable a correction for time-dependent degradation (Section 3.8).



185
186 **Figure 1.** Flow chart for retrieving ozone profiles with optimal estimation-based inversion.

187

188 **This OE-based inversion** is physically regularized toward minimizing the difference between a
189 measured spectrum \mathbf{Y} and a spectrum that is simulated by the forward model $\mathbf{R}(\mathbf{X})$, constrained by
190 measurement error covariance matrix \mathbf{S}_y and statistically regularized by an a priori state vector \mathbf{X}_a and
191 error covariance matrix \mathbf{S}_a . The solution at iteration step $i + 1$ is written as

$$192 \quad \mathbf{X}_{i+1} = \mathbf{X}_i + (\mathbf{K}_i^T \mathbf{S}_y^{-1} \mathbf{K}_i + \mathbf{S}_a^{-1})^{-1} [\mathbf{K}_i^T \mathbf{S}_y^{-1} (\mathbf{Y} - \mathbf{R}(\mathbf{X}_i)) - \mathbf{S}_a^{-1} (\mathbf{X}_i - \mathbf{X}_a)], \quad (1)$$

193 where each component of \mathbf{K} is the derivative of the forward model, called the Jacobians or weighting
194 function matrix. \mathbf{Y} is composed of the logarithm of the sun-normalized radiance. To construct \mathbf{S}_y , the
195 normalized random-noise errors of radiance and irradiance taken from OMI L1b products are summed
196 up as total measurement errors. The measurement errors are typically underestimated and then noise
197 floors (0.4 % below 310 nm, 0.15-0.2% above) are imposed on as a minimum value. **Note that** \mathbf{S}_y is a
198 diagonal matrix, assuming that measurement errors are uncorrelated among wavelengths.

199 The optimal estimate is iteratively updated until convergence when the relative change in the cost
200 function between previous and current iterations is less than 1.0 %. The cost function χ^2 is given by

$$201 \quad \chi^2 = \left\| \mathbf{S}_y^{-\frac{1}{2}} \{ \mathbf{K}_i (\mathbf{X}_{i+1} - \mathbf{X}_i) - [\mathbf{Y} - \mathbf{R}(\mathbf{X}_i)] \} \right\|_2^2 + \left\| \mathbf{S}_a^{-\frac{1}{2}} (\mathbf{X}_{i+1} - \mathbf{X}_a) \right\|_2^2 \quad (2)$$

where $\| \cdot \|_2^2$ denote the sum of each element squared. Maximum number of iterations is set to be 10 against the divergence. Typically, it takes 2-3 iterations to converge, but increasing to 6-7 for thick clouds.

~~The state vector~~ Table 2 provides fitting variables for OMPROFOZ v2, along with their a priori values and a priori errors. ~~In s to be fitted in OMPROFOZ v2 are listed in Table 2, together with their a priori value and a priori error. comparison~~ Compared to the OMPROFOZ v1 previous version, three kinds of parameters are newly added to implement the slit function linearization (slit width coefficient, shape factor coefficient) and common mode correction as a pseudo absorber. A priori value and error are set empirically for spectroscopic parameters, and are taken from climatological datasets for geophysical parameters such as atmospheric ozone and surface albedo. They are assumed to be uncorrelated between ~~fitting parameters~~ fitting parameters, except for atmospheric profiles a priori ozone error covariance matrix with ~~at~~ the correlation length of 6 km, which gives $S_a(i, j) = \sigma_i^a \sigma_j^a \exp(-|i - j|/6)$, where σ^a is a priori error, with i and j being layer numbers. Cloud fraction is initially taken from OMCLDO2 and fitted at 347 nm together with initial surface albedo taken from OMLER.

Table 2. List of fitting variables, a priori values and a priori errors. A correlation length of 6 km is used to construct the a priori covariance matrix for ozone variables. All the other variables are assumed to be uncorrelated with each other.

Fitting variables	# Variables	A priori	A priori error
Ozone at each layer	24	Climatology	Climatology
Surface albedo	2 (1 for each channel)	Climatology	0.05
First-order wavelength-dependent term for surface albedo	1 (only UV2)	0.0	0.01
Cloud fraction	1 (only UV2)	Derived from 347 nm	0.05
Radiance/irradiance wavelength shifts	2 (each channel)	0.0	0.02 nm
Radiance/O ₃ cross section wavelength shifts	2 (each channel)	0.0	0.02 nm
Ring scaling parameters	2 (each channel)	-1.87	1
offset parameters in radiance	2 (each channel)	0.0	1.0 ⁻⁴
[±] Slit width coefficient	2 (each channel)	0.0	0.1 nm
[±] Shape factor coefficient	2 (each channel)	0.0	0.1
[±] Common mode scaling parameter [±]	2 (each channel)	1.0	1.0

[±]New variables incorporated into the OMPROFOZ v2 algorithm.

2.3 OMPROFOZ product

The previous version product was stored in the HDF-EOS5 format, but the NetCDF-4 format is applied to create the OMPROFOZ v2 product, similar to other collection 4 OMI data products. Also, it is written using the TEMPO output libraries so that it shares common data structures and metadata definitions with TEMPO data products.

The main product parameters are partial ozone columns at 24 layers, ~ 2.5 km for each layer, from the surface to ~ 65 km in the unit of Dobson Unit (DU, $1 \text{ DU} = 2.69 \times 10^{16} \text{ molecules.cm}^{-2}$). The 25-level vertical pressure grid is set initially at $P_i = 2^{-i/2}$ atm for $i=0, 23$ and with the top of the atmosphere set for P_{24} . This pressure grid is then modified: the surface pressure and the thermal tropopause pressure are used to replace the level closest to each one, and tropospheric layers are distributed equally with logarithmic pressure. Correspondingly, the random-noise error and solution error profiles are provided in terms of a square root of diagonal elements of random-noise error covariance matrix \mathbf{S}_n and solution error covariance matrix $\hat{\mathbf{S}}$ that is directly estimated from the retrievals:

$$\mathbf{S}_n = \mathbf{G}\mathbf{S}_y\mathbf{G}^T, \hat{\mathbf{S}} = (\mathbf{K}^T\mathbf{S}_y^{-1}\mathbf{K} + \mathbf{S}_a^{-1})^{-1}, \text{ and } \mathbf{G} = \hat{\mathbf{S}}\mathbf{K}^T\mathbf{S}_y^{-1}, \quad (3)$$

where \mathbf{G} is the matrix of contribution functions. The smoothing error covariance \mathbf{S}_s can be also directly estimated, but is not provided in the output file. That is because it can be derived with the following relationship:

$$\hat{\mathbf{S}} = \mathbf{S}_s + \mathbf{S}_n. \quad (4)$$

$$\mathbf{S}_s = (\mathbf{A} - \mathbf{I})\mathbf{S}_a(\mathbf{A} - \mathbf{I})^T, \quad (5)$$

where \mathbf{I} is the unit vector and \mathbf{A} is the matrix of averaging kernels:

$$\mathbf{A} = \frac{\partial \mathbf{x}}{\partial \mathbf{x}_T} = (\mathbf{K}^T\mathbf{S}_y^{-1}\mathbf{K} + \mathbf{S}_a^{-1})^{-1}\mathbf{K}^T\mathbf{S}_y^{-1}\mathbf{K} = \hat{\mathbf{S}}\mathbf{K}^T\mathbf{S}_y^{-1}\mathbf{K} = \mathbf{G}\mathbf{K}. \quad (6)$$

A particular row of \mathbf{A} describes how the retrieved profile in a particular layer is affected by changes in the true profile in all layers. It is a very useful variable to characterize the retrieval sensitivity and vertical resolution of the retrieved profile. The diagonal elements of \mathbf{A} , known as Degrees of Freedom for Signal (DFS) represent the number of useful independent pieces of information available at each

256 layer from the measurement. To quantify the performance of the spectral fitting, the mean fitting
 257 residuals are calculated for each fitting window (UV1, UV2), in the form of the root mean square of
 258 spectral differences relative to the measured spectrum and the measured error as follows:

259

$$260 \quad \text{RMS} = \sqrt{\frac{1}{N} \sum_1^N ((I_m - I_s)/I_m)^2} \times 100 (\%), \text{ and } \text{RMSE} = \sqrt{\frac{1}{N} \sum_1^N ((I_m - I_s)/I_e)^2} \quad (7)$$

261

262 where I_m , I_s , and I_e represent measured spectrum, simulated spectrum, and measured errors,
 263 respectively, with N the number of the wavelengths in each window. The RMS of fitting residuals needs
 264 to be better than 0.2-0.3 % in the Huggins band (310-340 nm) for reliable retrievals of tropospheric
 265 ozone (Munro et al., 1998). The RMSE describes both spectral fit quality and the stability of
 266 regularization. The ideal value of RMSE is one. If $\text{RMSE} \ll 1$, either the fitting is overfitted or the
 267 measurement errors are overestimated. On the other hand, if $\text{RMSE} \gg 1$, either the fitting is underfitted
 268 or the measurement errors are underestimated.

269

270 **4.3. Specification and verification of updated implementations**

271

272 This section specifies new and improved updates made in the OMPROFOZ algorithm, listed in
 273 Table 3. The corresponding impacts on the spectral fit and ozone retrievals are verified. Note that the
 274 verification results of several implementations have already been presented in companion papers
 275 indicated in the fourth column of Table 3, which is briefly described in this paper. The unpublished
 276 implementations are specifically described in this paper.

277

278 **Table 3.** Lists of updates on algorithm implementations

Implementations	OMPFOZ v1	OMPFOZ v2	Verification
A priori ozone climatology	Latitude dependent monthly profiles	Latitude and tropopause (daily) dependent monthly profiles	Bak et al. (2013)
Meteorological data	NCEP	OMUFPSLV OMUFPMET	This work
Irradiance	Climatological composite	Monthly composite	This work
Solar reference spectrum	Chance and Kurucz (2010)	Coddington et al. (2021)	Bak et al. (2022)
Slit function	Gaussian parameterization	Super Gaussian parameterization and linearization	Bak et al. (2019b)
Ozone cross section	BDM (Brion et al., 1993; Daumont et al., 1992; Malicet et al., 1995)	BW (Birk and Wagner, 2018)	Bak et al. (2020)
Radiative transfer calculation	VLIDORT only	PCA-VLIDORT	Bak et al. (2021)
Radiometric	CCD dependent soft calibration	- CCD and time	This work

calibration		dependent soft calibration - Common mode correction	
-------------	--	--------------------------------------------------------------	--

279

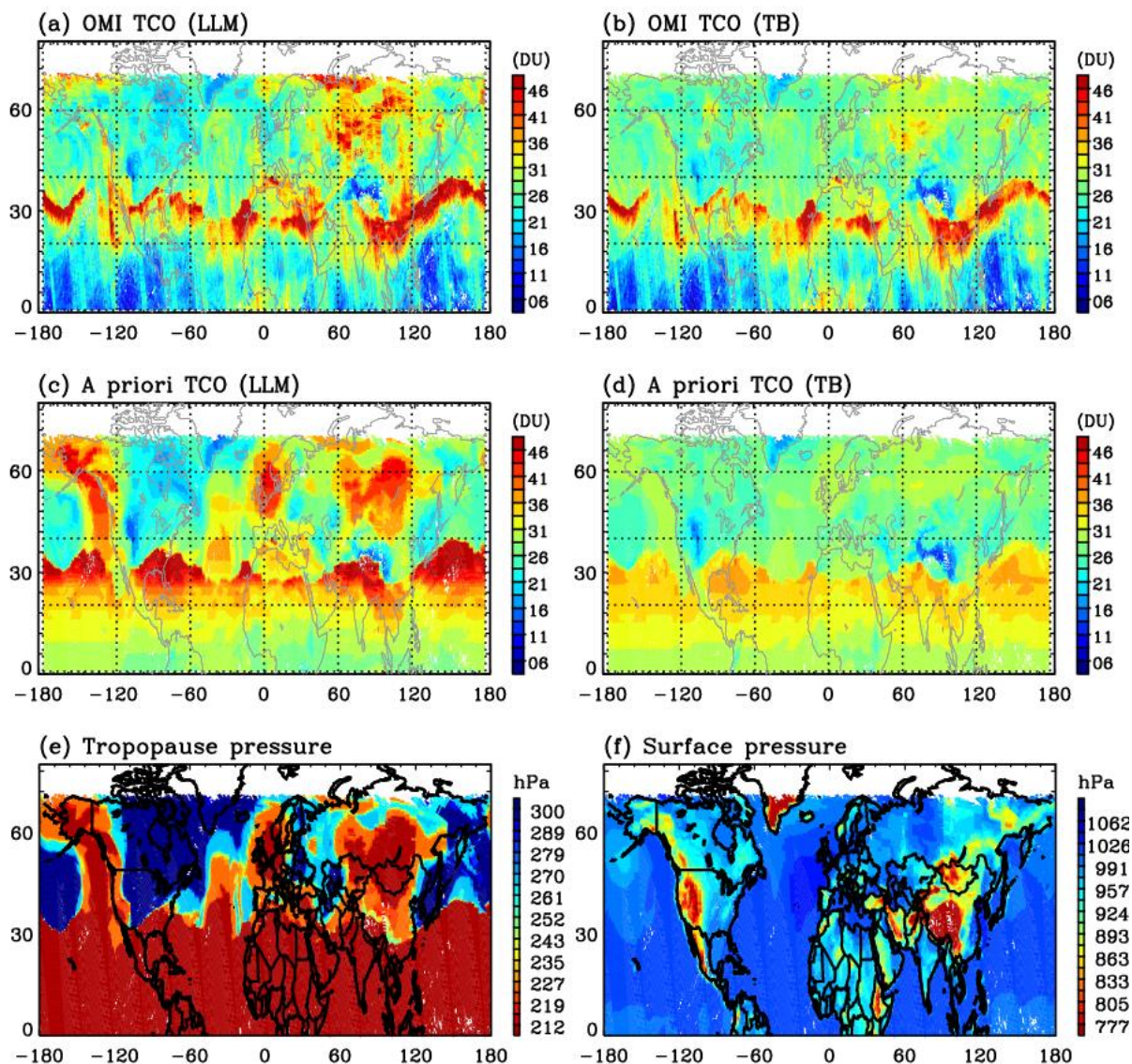
280 3.1 A priori ozone climatology

281 An ~~optimal-estimation~~OE-based ozone retrieval can be significantly affected by the quality of a
282 priori data given insufficient measurement information. Therefore, the constraint can push the retrieval
283 away from the actual state of the atmosphere towards a priori information, especially near the boundary
284 layer or the tropopause where the vertical resolution of nadir satellite observations is inherently limited.
285 In the v1 algorithm, the a priori ozone information was taken from McPeters et al. (2007) (abbreviated
286 as LLM climatology) consisting of monthly average ozone profiles for every 10°-latitude zone based
287 on ozonesonde measurements in the troposphere and lower stratosphere and satellite measurements
288 above. The v2 algorithm implements a tropopause-based (TB) ozone profile climatology from which a
289 zonal monthly mean profile is vertically adjusted according to the tropopause height taken from the
290 daily meteorological database described in Sect. 3.2. Applying the TB climatology as OMI a priori was
291 thoroughly verified in Bak et al. (2013) who demonstrated improvements of OMI ozone profile
292 retrievals in comparison with ozonesondes as well as in representing the sharp gradients of ozone
293 vertical structures near the tropopause. Figure 2 compares tropospheric ozone retrievals on 01 February
294 2007 with a priori ozone constraints being taken from LLM and TB, respectively. The most noticeable
295 difference is identified in the northern region of Europe where abnormally high concentrations are
296 retrieved when LLM is used as a priori. This retrieval issue was also mentioned in comparing
297 OMPROFOZ v1.0 with other satellite products, data assimilation, and chemical transport model
298 calculation (Gaudel et al., 2018; Ziemke et al., 2014), showing large positive biases in tropospheric
299 column ozone during high-latitude winter, but it has not been explained. It is clearly seen that the
300 abnormal feature of the retrieved high ozone is closely correlated with the high LLM a priori (Fig. 2.c)
301 resulting from abnormally low tropopause pressure or high tropopause height (Fig. 2.e). LLM can
302 represent the typical vertical profiles whose ozonepause is located at ~ 8 km over high latitudes during
303 the winter. Therefore, with the presence of the abnormally high tropopause height, the lower
304 stratospheric layers of LLM profiles can be misrepresented as a priori in the upper tropospheric ozone
305 layers, which likely causes the large positive biases of ozone retrievals in the troposphere seen in
306 OMPROFOZ v1. However, an ozone profile taken from the TB climatology is re-distributed according
307 to the daily tropopause which becomes an ozonepause of TB profiles. In the subtropical region, LLM
308 may also provide incorrect information in the presence of high tropopause height, but ozone retrievals
309 are less affected, implying that OMI retrievals are less constrained by the a priori information in this

310 case due to more measurement information, unlike in the northern high-latitudes.

311

312

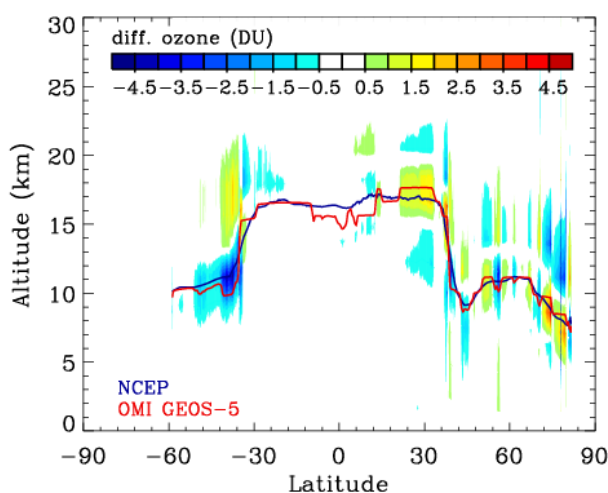


313

314 **Figure 2.** Comparison of (a,b) OMI tropospheric column ozone (TCO) and (c,d) the corresponding a priori TCO
315 taken from monthly and zonal mean climatologies (LLM/left, TB/right), respectively, in the Northern hemisphere
316 on 01 February 2007. (e) tropopause and (f) surface pressure fields are presented in the bottom panels. - It is noted
317 that the meteorological fields are commonly taken from the NCEP reanalysis data to see the impact of applying
318 different A priori ozone data on the retrieval.
319

320 3.2 Meteorological data

321 As a forward model input, the surface pressure is required to define the bottom of the atmosphere,
 322 with the air temperature profile to account for the temperature dependence of the ozone absorption cross
 323 section, especially in the Huggins band. The tropopause pressure is also required to be used as one of
 324 the retrieval vertical levels to separate stratospheric ozone from tropospheric ozone, and determine the
 325 a priori ozone profile in the case of using the TB climatology ~~in v2Version-1~~. In Vversion-1, tThese
 326 meteorological variables were taken externally from National Centers for Environmental Prediction
 327 (NCEP) reanalysis data (<http://www.cdc.noaa.gov>), which provide 6-hourly (4 time a day) global
 328 analyses at $2.5^\circ \times 2^\circ$ grids with 17 vertical pressure levels below 10 hPa. These databases were pre-
 329 interpolated to 1:45 PM local solar time when OMI is crossing at equator and OMI's ground pixels
 330 using nearest neighbor interpolation and then manually transmitted to OMI SIPS. However, the data
 331 transmission has been accidentally halted since June 2011 and hence climatological monthly mean data
 332 have been used as a back-up in the data processing. To avoid this risk, the meteorological input is
 333 switched to the internal meteorological products, geo-located to OMI UV-2 1-Orbit L2 Swath from
 334 the 2D Time-Averaged Single-Level Diagnostics (OMUFPSLV) (Joiner, 2023a) and the GEOS-5 FP-
 335 IT 3D Time-Averaged Model-layer Assimilated data (OMUFPMET) (Joiner, 2023b). We take the
 336 ~~average~~ air temperatures given at 72 pressure levels above the center of the ground pixel from
 337 OMUFPMET as well as surface temperature, surface pressure, and thermal tropopause pressure at the
 338 center of the ground pixel from OMUFPSLV. The impact of switching meteorological input on the
 339 spectral fitting residuals is insignificant (not shown here), implying that the residuals might be absorbed
 340 by other state vectors. Figure 3 illustrates that ozone profile retrievals are changed by 2-3 DU, especially
 341 in the tropopause region due to changes of a priori ozone profiles in adjusting the climatological TB
 342 ozone profile around the daily tropopause height.



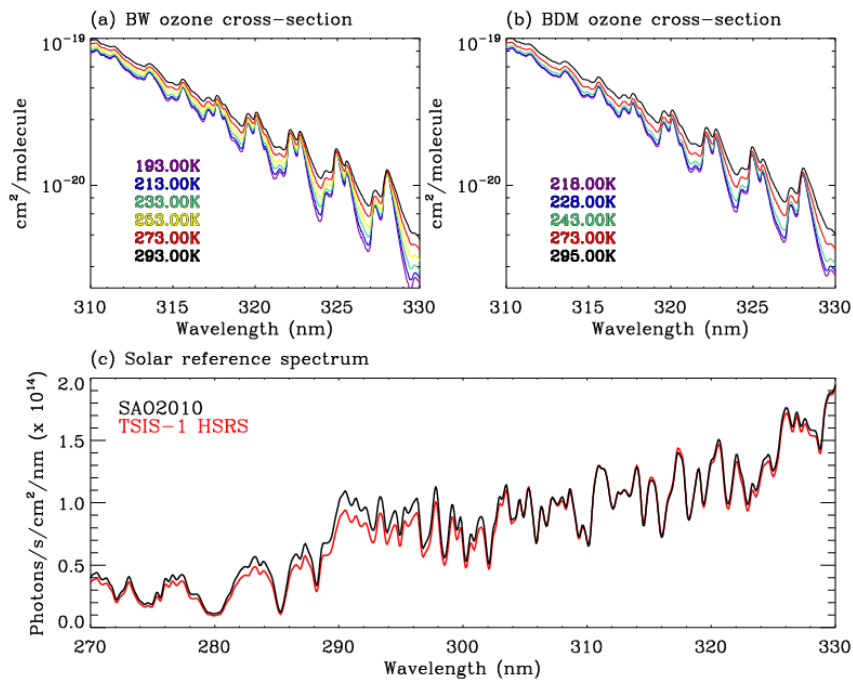
343
 344 **Figure 3.** Differences of OMI ozone profile retrievals (DU) along the nadir view from 7th orbit of measurements
 345 on 15 Jun 2006, due to switching the meteorological input from NCEP to OMI GEOS-5 (OMUFPSLV and

346 OMUFPMET). The solid line represents the tropopause height from NCEP (blue) and OMI GEOS-5 (red).

347

348 3.3 Ozone cross section

349 The BDM cross-section measurements have been the standard input for retrieving ozone profiles
350 using BUV measurements over the last decade (Liu et al., 2013, 2007; Orphal et al., 2016). In a
351 companion paper (Bak et al., 2020), the new BW ozone cross-section dataset was tested to check if
352 there is room to improve our ozone profile retrievals, which made us switch the cross section from
353 BDM to BW in OMPROFOZ v2. As illustrated in Figure 4 (upper), the BW dataset provides improved
354 temperature coverage from 193 K to 293 K, every 20 K over the BDM dataset given only at five
355 temperatures above 218 K. Therefore, BW measurements were better parameterized as quadratic
356 temperature-dependent coefficients with uncertainties of 0.25-2 % whereas for BDM measurements
357 fitting residuals of 2-20 % remains. Note that parameterized coefficients of cross-section measurements
358 are typically applied in both column ozone and ozone profile retrievals for conveniently representing
359 the temperature dependence of cross-section spectrum. Bak et al. (2020) also showed a large impact of
360 switching cross-sections on ozone profile retrievals when soft calibration is turned off. With soft
361 calibration derived using consistent cross sections, some of the systematic differences due to cross
362 sections can be greatly reduced; using BW can still improve the retrievals due to its better temperature
363 dependence, but it does not cause the most impactful changes.~~Bak et al. (2020) also demonstrated the~~
364 ~~improved performance of ozone profile retrievals through comparison with ozonesonde measurements,~~
365 ~~showing a significant reduction of the standard deviations, by up to 15 % in the lower stratosphere and~~
366 ~~upper troposphere where atmospheric temperatures are lower than ~200 K.~~



367

368 **Figure 4.** Comparisons of (a,b) ozone cross-sections and (c) solar reference spectrum used in OMPROFOZ v1
 369 and v2 algorithms. Note that high-resolution solar reference spectrum is convolved with a Gaussian slit function
 370 of 0.4 nm FWHM (Full Width at Half Maximum) resolution.

371

372 **3.4 High-resolution solar reference spectrum**

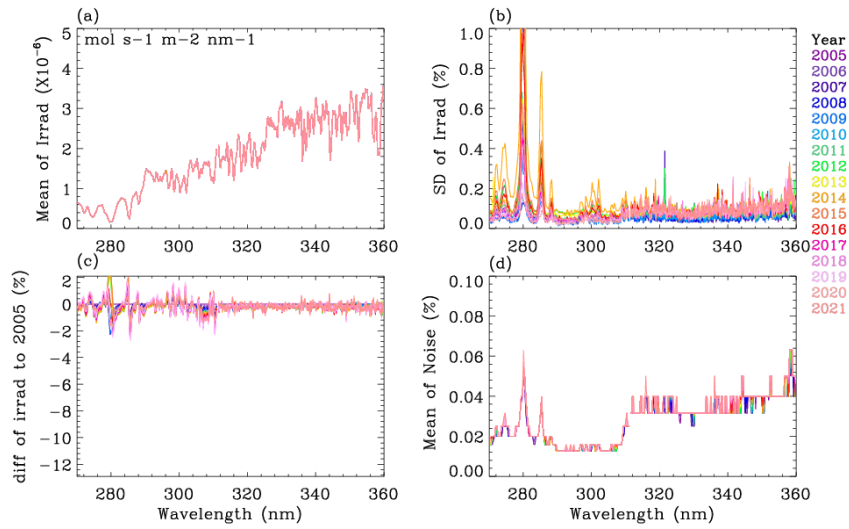
373 An accurate, high-resolution extraterrestrial solar reference spectrum is required for either wavelength
 374 calibration or slit function characterization. We decided to switch the solar reference spectrum from
 375 Chance and Kurucz, (2010) to Coddington et al., (2021). Figure 4.c illustrates radiometric discrepancies
 376 between the new solar reference called the TSIS-1 Hybrid Solar Reference Spectrum (HSRS) and the
 377 old solar reference called the SAO2010. A companion paper evaluated that the radiometric uncertainties
 378 of the new reference spectrum are below $\sim 1\%$ whereas for SAO2010 those range from 5% in the
 379 longer UV part to 15% in the shorter UV part (Bak et al., 2022). Furthermore, they confirmed an
 380 opportunity to improve the spectral fitting of slit functions and hence the spectral fitting of ozone when
 381 using the TSIS-1 spectrum; the impact on ozone profile retrievals is 5-7% in the troposphere.

382

383 **3.5 Solar irradiance spectrum**

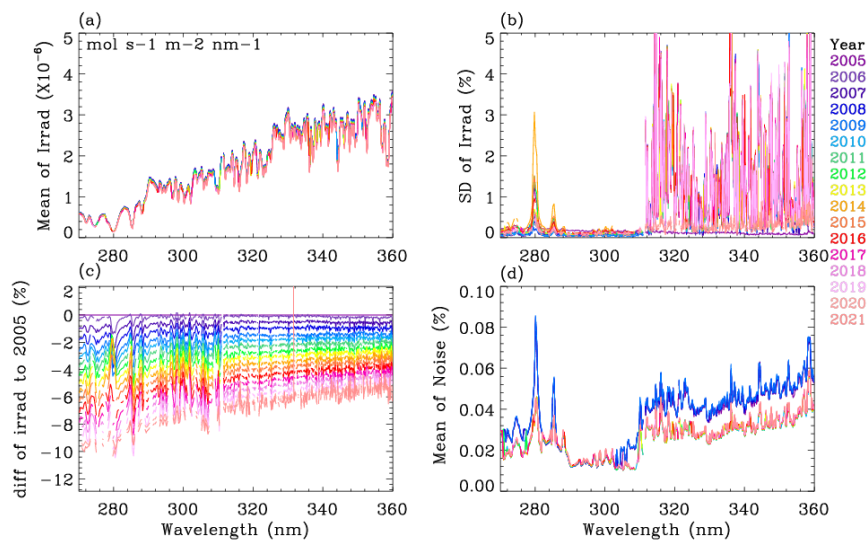
384 OMI makes solar irradiance measurements near the northern hemisphere terminator of an orbit once
 385 per day, which are required to calculate top-of-atmosphere reflectance and to estimate an on-orbit slit

386 function in ozone profile retrievals. In order to reduce the short-term noise of ~~OMI~~ individual
387 measurements, the ~~v1.0~~earlier algorithm implemented the use of climatological solar spectra derived
388 from three years of daily OMI Level 1B product (2005-2007). In the ~~v2.0~~newer algorithm, collection 4
389 irradiance spectra are tabled as a monthly average to ~~reduce either~~ the short-term noise as well as ~~cancel~~
390 ~~out~~address seasonal variations of instrument characteristics that are the common in both degradation
391 existing in radiance and irradiance measurements. Figures 5 and 6 compare irradiance measurements
392 averaged over July for each year from collection 4 and collection 3, respectively. Collection 3 shows
393 significant short-term noise in daily measurements in the UV2 range, around 3-5 % and also
394 systematically decreasing patterns of monthly irradiance spectra from - 10 % in the UV1 range and -
395 6 % in the UV2 range over the mission. Collection 4 provides much improved irradiance spectra with
396 respect to both degradation and noise errors. In addition, OMI random-noise errors in the monthly
397 average spectra are compared. Collection 4 ranges from 0.02 % in the UV1 and 0.04 % in the UV2,
398 consistently over the mission. However, collection 3 shows somewhat different features in the UV2
399 range, like more wavelength dependence and a systematic drift as of 2008-2009. Figure 7 shows the
400 impact of switching OMI level1b product from collection 3 to 4 on fitting residuals resulting from ozone
401 profile retrievals on 16 July 2020; the average fitting residuals are plotted as a histogram for each fitting
402 window. In this experiment, the v2 implementations are identically applied without radiometric
403 corrections (soft calibration and common mode correction are turned off). In addition, the impact of
404 using monthly and daily irradiance is investigated. As shown, fitting residuals are noticeably improved
405 in both fitting windows due to switching from collection 3 to 4. This experiment illustrates that monthly
406 irradiances should be used instead of daily measurements when using the collection 3 product. In
407 comparison, the corresponding impact on fitting residuals with collection 4 product is not very
408 significant due to improvements of short-term noise errors in daily irradiance measurements, but the
409 number of retrievals with smaller fitting residuals increases in the UV2 band.



410

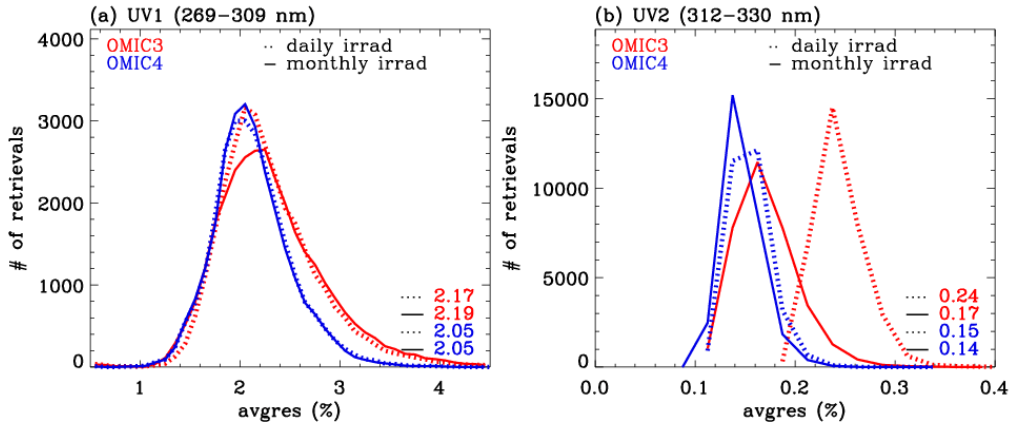
411 **Figure 5.** (a) Monthly mean irradiance spectra of OMI collection 4 product in July from 2005 to 2021 at the
 412 10th cross-track position for UV-1 band and 20th cross-track position for UV-2 band without coadding. (b)
 413 Corresponding standard deviations of the monthly mean irradiances, (c) Biases of the mean irradiances relative
 414 to 2005, and (d) Monthly mean random noise errors.



415

416 **Figure 6.** Same as Figure 5, but for OMI collection 3 irradiance product.

417



418

419 **Figure 7.** Histograms of average fitting residuals from OMI collection 3 (red) and 4 (blue) level 1b products on
 420 15 July 2020, in (a) UV1 and (b) UV2 ranges, respectively. In order to make a fair comparison, this experiment
 421 limits OMI measurements to the western side of the swath to avoid using row anomaly cross-track pixels and
 422 empirical recalibration is not applied. Fitting residuals are evaluated with both daily (dashed) and monthly mean
 423 (solid) OMI irradiance measurements. The median values of average fitting residuals are presented in the legend.

424

425 3.6 Instrument spectral response function (ISRF) parameterization and linearization

426 OMI ISRFs were previously parameterized as a standard Gaussian by fitting the slit width (w) from
 427 OMI solar irradiances separately for each channel and each cross-track position. In the updated
 428 implementation, one more parameter, shape factor (k) is added to parameterize ISRFs as a Super
 429 Gaussian ($S(\Delta\lambda) = \exp\left[-\left|\frac{\Delta\lambda}{w}\right|^k\right]$). However, slit functions in radiance could deviate from those
 430 derived from solar spectra due to the sensitivity to scene heterogeneity, differences in stray light between
 431 radiance and irradiance, and intra-orbit instrumental changes. These might cause some spectral
 432 structures in the radiance fitting. Therefore, the v2 algorithm treats these spectral errors as Pseudo
 433 Absorbers (PAs), which is derived as $\frac{\partial I}{\partial p} = -\frac{\partial S}{\partial p} \otimes I_{\pi}$ ($p = w$ or k) through the slit function linearization.
 434 As specified in Table 2, these PAs are iteratively adjusted with zero-order scaling parameter. These PA
 435 coefficients are weakly correlated with ozone variables, except for the UV2 shape factor coefficient
 436 (Δk) and tropospheric ozone (0.2-0.3). The description and evaluation of this implementation for OMI
 437 ozone profile retrievals is detailed in a companion paper (Bak et al., 2019b).

438

439 3.7 Radiative Transfer Calculation

440 The radiative transfer (RT) model is needed for calculating the forward model component such as top-
 441 of-the-atmosphere radiances, and Jacobians of radiances with respect to the atmospheric and surface

442 parameters. The radiance calculation is made for a Rayleigh atmosphere (no aerosols) with Lambertian
 443 reflectance assumed for the surface and for clouds. The Independent Pixel Approximation (IPA) is
 444 employed to treat partial clouds by assuming a cloud reflectivity of 80 %: $I = I(R_{sfc}, P_{sfc})(1 - f_c) +$
 445 $I(R_{cloud}, P_{cloud}) f_c$ where R and P represent reflectivity and pressure at bottom level (surface or cloud)
 446 with f_c as an effective cloud fraction. According to the Nyquist criterion (Goldman, 1953), individual
 447 spectra need to be simulated at grid spacings finer than a minimum of two pixels (four pixels in practice)
 448 per spectral resolution. Individual radiances need to be simulated at finer grids than at least 4 pixels per
 449 FWHM so that the spectral convolution is applied to account for OMI spectral resolution. To reduce the
 450 computational burden, a few wavelengths are effectively selected (λ_e) for running RT model and then
 451 interpolated to regular high-resolution grids (λ_h) with the radiance adjustment for errors caused by the
 452 spectral resolutions as follows:

$$453 \quad I(\lambda_h) = I(\lambda_e) + \sum_{l=1}^N \frac{\partial I(\lambda_e)}{\partial \Delta_l^{gas}} \left(\Delta_l^{gas}(\lambda_h) - \Delta_l^{gas}(\lambda_e) \right) + \frac{\partial I(\lambda_e)}{\partial \Delta_l^{ray}} \left(\Delta_l^{ray}(\lambda_h) - \Delta_l^{ray}(\lambda_e) \right), \quad (7)$$

454 where $\frac{\partial I}{\partial \Delta_l}$ represents for Jacobians with respect to optical properties at layers l ($l = 1$ to N). In the v2
 455 forward model, both λ_c and λ_h are set to be finer than intervals previously used as noted in Table 4
 456 where the implementation details between v1 and v2 forward models are compared. To accelerate ~~RT~~
 457 forward model calculations, the RT model has been is switched from the earlier version 2.4 of
 458 VLIDORT v2.4 to a newer PCA-based VLIDORT model (version 2.8). Formerly, multiple scattering
 459 (MS) calculations are performed at individual wavelengths, in the former whereas in the newer model
 460 MS calculations in the latter are performed-carried out only for a few EOF-derived optical states which
 461 are developed from spectrally binned sets of inherent optical properties that possess some redundancy.
 462 In both these VLIDORT-based forward models, v1 and v2 forward models, the polarization is not
 463 accounted for part of the direct RT simulation of the entire spectrum; but a polarization instead,
 464 polarization correction is applied to speed up the RT. In the ~~v1-earlier~~ forward model, vector calculations
 465 are additionally executed at 14 wavelengths to ~~calculate-establish 14~~ the scalar vs. vector intensity
 466 differences ~~at these wavelengths~~ which are then interpolated to every-all other wavelengths. However,
 467 residual polarization errors remain, along with other approximation-forward model errors arising from
 468 using-the use of a low number of discrete ordinates (4 half-streams in each polar hemisphere) and
 469 relatively coarse vertical layerlayerings (~ 2.5 km thick). The ~~v2-newer~~ forward model reduces the
 470 number of half-space discrete ordinate streams from 4 to 2, and this with a resulting-increases in the
 471 speed ~~of-by~~ a factor of ~ 2 . To ~~eliminate-compensate for~~ the resulting-increase in RT approximation
 472 errors, a look-up table (LUT)-based correction is performed; this corrects, ~~which enables to for~~ adjust
 473 the differences in RT variables due to the number of different number of streams-discrete ordinates (2
 474 vs. 6) and number of layers (24 vs. 72) as well as correcting for neglecting-the neglect of polarization

effect. As ~~verified-described~~ in a companion paper, [these](#) updates improve the retrieval speed by a factor of ~ 3.3 as well as the retrieval accuracy (Bak et al., 2021). Note that the Ring simulation remains unchanged from v1 algorithm; the spectral structure of the Ring signal is externally simulated with the iterative fitting of amplitude of the Ring spectrum and then subtracted from the measured spectral reflectance ([Liu et al. 2010](#)).

Table 4. Comparison of implementation details for forward model simulation.

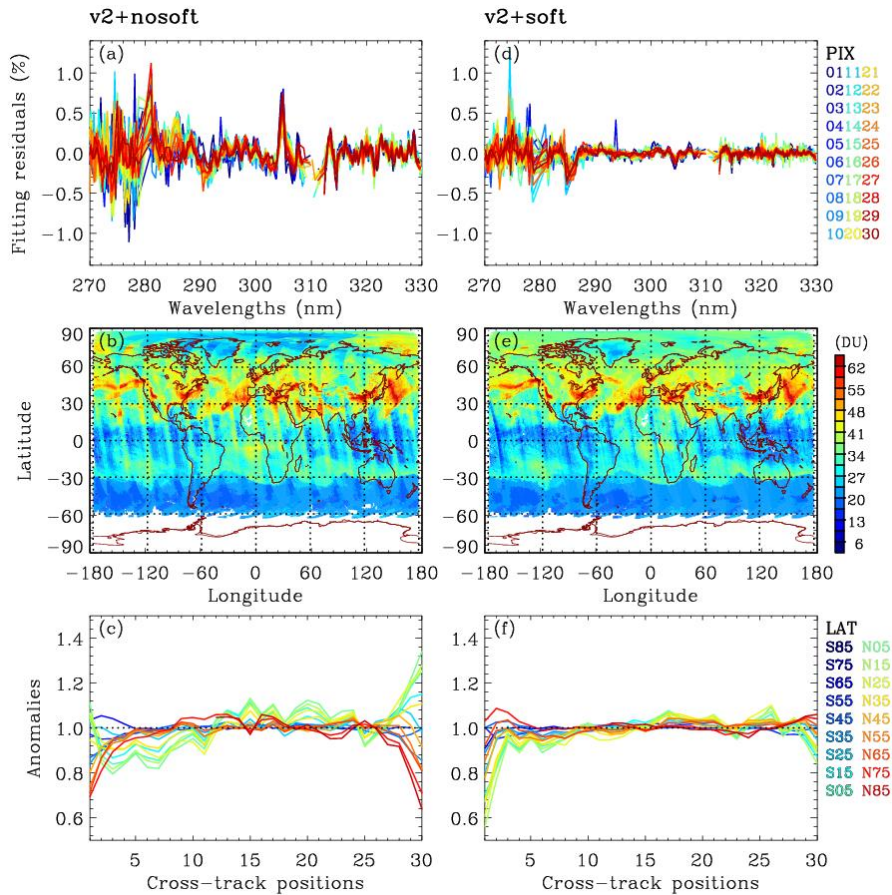
	V1	V2
λ_c	295nm 310nm 1.0 0.4 0.6	305 nm 0.3 0.1
λ_h	0.05 nm	0.03 nm
RT model	VLIDORT 2.4	PCA-based VLIDORT v2.8
N_{stream}^*	4	2
N_{stokes}	1 (scalar)	1 (scalar)
N_{layer}	24	24
RT correction	On-line polarization correction	LUT-based correction

*The N_{stream} is the number of discrete ordinate streams in the half-space.

3.8 Soft calibration

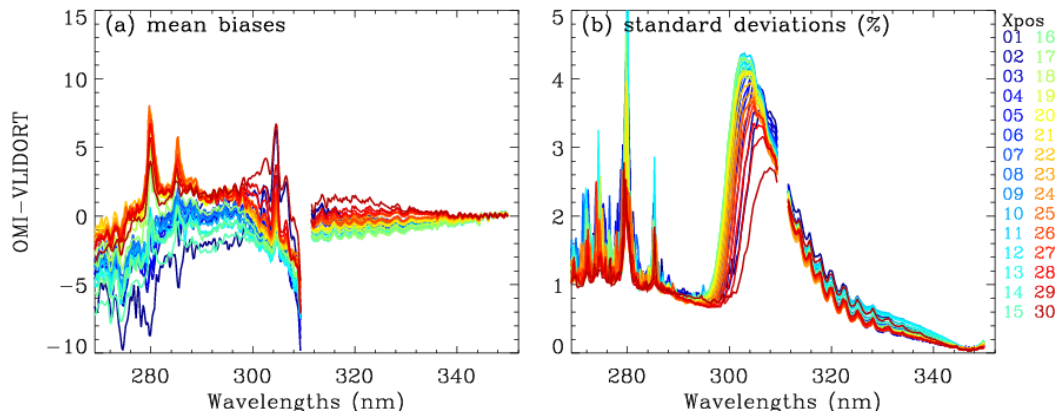
The left panels of Figure 8 show (a) the spectral fitting residuals averaged in the latitude band of 60°S to 60°N, (b) tropospheric column ozone (TCO) distribution, and (c) cross-track dependent stripe errors of TCOs where OMI collection 4 L1b product is applied without any radiometric corrections. As shown, there remain quite persistent residuals of up to $\sim 1.0\%$ in the UV1 range and of up to 0.3% in the UV2 range. The TCO distribution shows the along-track stripes that are commonly found in OMI trace gas products ([e.g., Kroon et al., 2008; Lamsal et al., 2021; Wang et al. 2016](#)). The cross-track dependent stripes of TCO are evaluated for 18 bands of latitude, as anomalies in the ratio of each cross-track column to the average column taken within cross-track positions 5-25 (1-based). The amplitude of anomalies is within $\pm 10\%$ at nadir pixels, but reaching to 40% at off-nadir pixels, with some dependency on latitudes. However, stratospheric column ozone (SCO) retrievals are almost free of stripe errors (not shown here). To reduce the striping, a soft calibration was applied to OMI radiances in OMPROFOZ v1. The soft spectra are derived as a systematic component of differences between measured and simulated radiances at tropical clear-sky pixels in summer where the forward model calculations are more accurate to attribute the residuals to measurement biases. The soft spectra are re-

498 derived for OMI collection 4 L1b product using the v2 forward model calculations (Sect 3.7). The ozone
499 profile input is prepared from 10-degree zonal averages of daily MLS measurements above 215 hPa
500 and climatological ozone profiles taken from McPeters and Labow (2012) below. In order to account
501 for the daily variability, the climatological profile shape is scaled to match total ozone value taken
502 from adjusted to account for the daily variability using 10-degree zonal averages of the level 3 OMI
503 TOMS-like total ozone product (OMTO3d). To smooth out the impact of daily ozone variabilities, one-
504 week measurements during July 11-17th over the tropics 20°S-20°N are used in deriving the soft spectra
505 after screening out outliers of extreme viewing geometries ($SZA > 60^\circ$), cloudy pixels ($f_c < 0.2$), bright
506 surfaces ($A_{sfc} > 0.1$), and aerosol contaminated pixels (aerosol index > 5) as well as abnormally large
507 values of average residuals ($UV1 > 8$, $UV2 > 3$). Note that the threshold value of filtering out aerosol
508 pixels needs to be relaxed due to the overestimation errors of aerosol index at initial iteration. Figure 9
509 displays the cross-track dependent soft spectrum for the case of July 2005 when instrument degradation
510 is negligible and row-anomaly damage has not occurred. It illustrates the existence of systematic
511 residuals between measured and simulated radiances within 2 % in UV2 and mostly from -7 to 3 % in
512 the UV1, except for some spikes. The right panels of Figure 8 demonstrate how soft calibration works
513 for improving ozone retrievals in comparison to the left panels where soft calibration is tuned off. It is
514 clearly shown that the systematic spikes are mostly eliminated as well as cross-track dependent stripes
515 are globally reduced even up to high-latitudes. In particular, the “anomalies” are reduced to within 0.1 %,
516 except at first cross-track pixels. This calibration has been applied independent of time and latitude in
517 the v1 algorithm. To account for OMI instrument degradation errors, the v2 soft spectra are developed
518 for every year. As an example, the yearly soft spectra are displayed at several cross-track positions in
519 Figure 10. There is noticeable yearly variation in the UV1 band, typically within 2-3% over 17 years.
520 The most significant degradation features are found at the first cross-track pixel in the UV1 band, with
521 relative change of 5 % or more. For cross-track positions 13, 18, 22, correction spectra cannot be derived
522 for most of the time periods after 2008 due to the occurrence of serious row anomaly. Although
523 correction can be derived for cross-track position 13 during 2020, it is significantly different from those
524 before 2008, indicating that it is still affected by row anomaly. The yearly variation in the UV2 band is
525 much smaller, and can be clearly identified below ~315 nm to be within 1 %. However, it could make
526 a significant impact on ozone profile retrievals because the spectral fit residuals need to be smaller than
527 0.2-0.3 % in the Huggins band for reliable retrieval quality of the tropospheric ozone (Munro et al.,
528 1998).



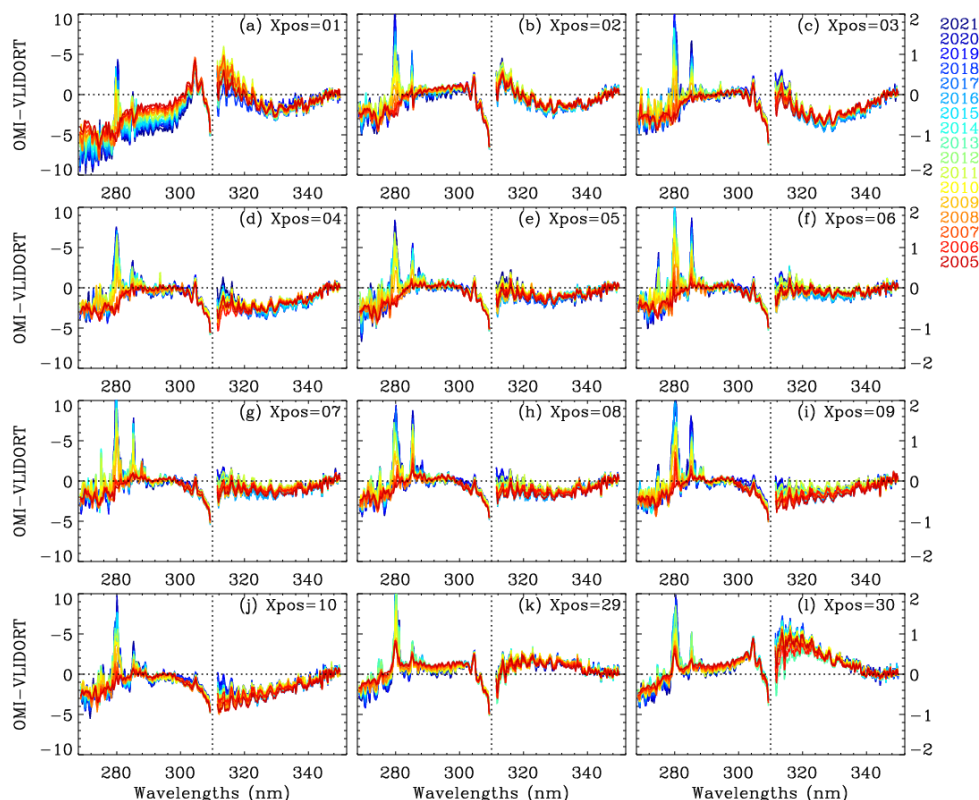
529

530 **Figure 8.** (a, d) Spectral fitting residuals (%) averaged in the latitude of 60°S and 60°N from OMI measurements
 531 on 15 June 2006, (b,e) the global distribution of tropospheric column ozone (TCO, DU), and (c,f) anomalies of
 532 TCO as a function of 18 latitude bands. Left and right panels are for without and with soft calibration, respectively.



533

534 **Figure 9** (a) soft calibration spectra derived for collection4 OMI L1b products in July 11-17, 2005,
 535 representing the systematic biases between measured and simulated spectrum. (b) the standard deviations of
 536 the systematic biases, representing the uncertainties of soft calibration spectra.



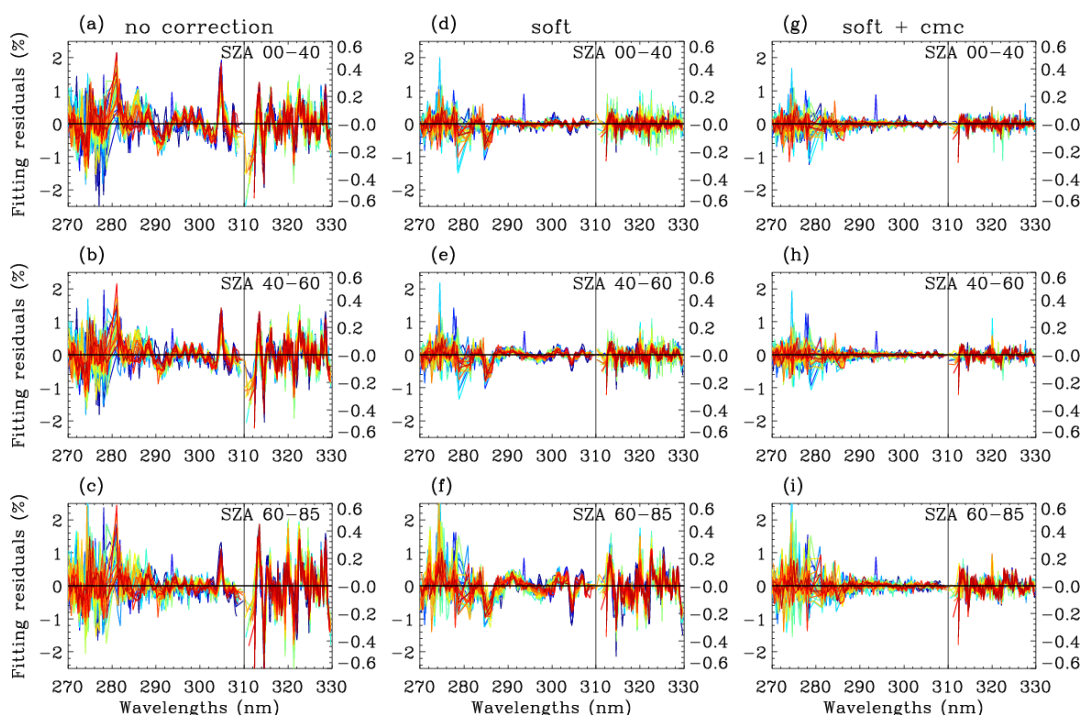
538

539 **Figure 10.** Yearly dependent soft calibration spectra from 2005 to 2021 at several cross-track positions (Xpos,
 540 UV1-based) which have been not affected by row anomalies over the mission. Note that the UV1 and UV2
 541 bands are plotted with different Y-axis ranges (left Y-axis for UV1 and right Y-axis for UV2) for better
 542 visualization.

543 3.9 Common mode correction

544 As compared in Figures 11 left and middle panels, the soft calibration is less effective in eliminating
 545 the systematic residuals at high solar zenith angles, especially in the UV2 band where the spectral
 546 residuals vary from 0.1 % at lower SZAs to 0.4 % at higher SZAs. This implies the existence of a
 547 spectral dependence of the radiometric calibration and detector sensitivity on the signal represented by
 548 solar zenith angle, which is not accounted for in the soft calibration dependent only on CCD dimension.
 549 ~~Moreover, the soft calibration induces the systematic errors spiking at around 285 nm and 305 nm in~~
 550 ~~the UV1 band. Therefore, A~~ common mode correction (CMC) is newly implemented in OMPROFOZ
 551 v2, to correct the remaining radiometric errors. The common mode spectrum of the fitting residuals is
 552 physically treated as a pseudo absorber, along with a scaling coefficient that is iteratively fitted in each
 553 of the UV1 and UV2 windows. Therefore, the scene-dependent radiometric errors could be partly

554 accounted for. This kind of correction is originally used in the spectral fitting process where a common
555 mode residual could be calculated on-line for each orbit of measurement. However, additional on-line
556 calculation is not practical for the time-consuming optimal estimation-based ozone profile retrieval
557 process. Therefore, we derive time-independent common mode spectra by averaging three days of
558 fitting residuals (July 13th -15th, 2005) over five solar zenith angle regimes [0° - 40° , 40° - 60° , 60° - 70° ,
559 70° - 80° , 80° - 85°] for each cross-track position. As demonstrated in Figure 11 right panel, the applied
560 common mode spectrum is likely to absorb the remaining spectral errors and hence the fitting accuracy
561 is globally improved. For example, the systematic features are clearly reduced above 285 nm in the
562 UV1 window, but the noisy features are still not well fitted below 285 nm. In the UV2 band, applying
563 CMC reduces the dependence of fitting residuals on both solar zenith angle and cross-track pixels and
564 hence the remaining residuals are globally less than 0.1 % at most wavelengths. As shown in Figures
565 12, striping patterns of tropospheric ozone retrievals could be reduced due to improvements of retrievals
566 at the first cross-track pixels in the tropics where soft calibration deepens anomalies (Figure 8.f).
567 Comparisons with OMPROFOZ v1 retrievals (Figure 12.d-f) demonstrate that OMPROFOZ v2 product
568 provides global information on tropospheric column ozone with smaller retrievals biases due to
569 radiometric calibration errors and more consistent data quality with respect to different viewing
570 geometries and latitude.



571
572 **Figure 11.** Comparison of spectral fitting residuals (%) averaged for three solar zenith angle regimes (00° - 40° ,
573 40° - 60° , 60° - 85°) from OMI measurements on 15 Jun 2005, with different radiometric calibration settings (left:

574 all radiometric correction is turned off, middle: soft calibration is turned on, right: soft calibration and common
 575 model correction are turned on). Note that the residuals are plotted in different y-axis range below (left y-axis)
 576 and above (right y-axis) 310 nm, respectively.

577

578 **4. Validation with ozonesonde measurements**

579 **Table 5.** lists of ozonesonde stations* and comparison statistics# of the tropospheric column ozone (900-
 580 200 hPa) between OMPROFOZ and ozonesondes

<u>Station</u>	<u>Hohenpeissenberg</u>	<u>Payerne</u>	<u>Uccle</u>
<u>Instrument</u>	<u>Brewer-Master</u>	<u>ECC⁺</u>	<u>ECC⁺</u>
<u>Country</u>	<u>Germany</u>	<u>Switzerland</u>	<u>Belgium</u>
<u>Lon, Lat (°)</u>	<u>11.01, 47.3</u>	<u>6.57, 46.49</u>	<u>4.35, 50.80</u>
<u>Elevation (km)</u>	<u>0.98</u>	<u>0.49</u>	<u>0.10</u>
<u>OMPROFOZ v1.0</u>			
<u>No. of comparison pairs</u>	<u>726</u>	<u>1025</u>	<u>893</u>
<u>Mean Bias ± 1σ (DU)</u>	<u>4.20±7.38 DU</u>	<u>2.22±6.85 DU</u>	<u>-0.74±6.08 DU</u>
<u>Mean Bias ± 1σ (%)</u>	<u>13.87±22.04%</u>	<u>7.50 ± 19.78 %</u>	<u>-0.81±17.34 %</u>
<u>Correlation coefficient</u>	<u>0.66</u>	<u>0.73</u>	<u>0.74</u>
<u>OMPROFOZ v2.0</u>			
<u>No. of comparison pairs</u>	<u>815</u>	<u>1084</u>	<u>946</u>
<u>Mean Bias ± 1σ (DU)</u>	<u>3.30±5.95 DU</u>	<u>0.99±5.15 DU</u>	<u>-2.09±5.12 DU</u>
<u>Mean Bias ± 1σ (%)</u>	<u>9.94±16.52%</u>	<u>2.87 ± 13.88 %</u>	<u>-5.11±13.05 %</u>
<u>Correlation coefficient</u>	<u>0.81</u>	<u>0.85</u>	<u>0.83</u>

581 5. *All data are downloaded from the World Ozone and Ultraviolet Data Center (WOUDC) data via <http://www.woude.org>.

582 6. ⁺Electrochemical concentration cell (ECC)

583 7. #The number of comparison pairs between OMI and ozonesonde during the period 2005 to 2020. Mean Biases and 1σ
 584 standard deviations are in both DU (Dobson Unit) and % from (OMI-ozonesonde) × 100/ozonesonde.

585 ~~Table 5. lists of ozonesonde stations* and comparison statistics# of the tropospheric column ozone~~
 586 ~~between PROFOZ v2.0 and ozonesondes~~

587 *All data are downloaded from the World Ozone and Ultraviolet Data Center (WOUDC) data via <http://www.woude.org>.

588 ⁺Electrochemical concentration cell (ECC)

589 #The number of collocations for comparison of the tropospheric column ozone (900-200 hpa) during the period 2005 to 2020.
 590 Mean Biases and 1σ standard deviations are in both DU (Dobson Unit) and % from (OMI-ozonesonde) × 100/ozonesonde.

591

592 Comparisons against ozonesonde measurements are performed to highlight improvements of data
 593 quality and long-term consistency of ~~OMOM~~PROFOZ v2 over ~~OMOM~~PROFOZ v1. Ozonesonde
 594 measurements are obtained from three sites over central Europe during the period of 2005 to 2020,
 595 listed in Table 5. Balloon-borne ozone profiles are regularly measured two/three times per week at these
 596 sites located close to each other. The coincidence criteria used to pair OMI and ozonesonde
 597 measurements are within 100 km and 6 hours and then the closest pair is selected after screening out
 598 row anomaly flagged pairs. For comparison, individual ozonesonde soundings are converted from mPa
 599 into DU and then interpolated at OMI vertical grids, but without adjusting the vertical resolution into
 600 OMI to address the total errors of OMI retrievals including smoothing errors. The relative difference is
 601 calculated as (OMI-ozonesonde)/ ozonesonde × 100 %. Extreme values that are beyond the mean by

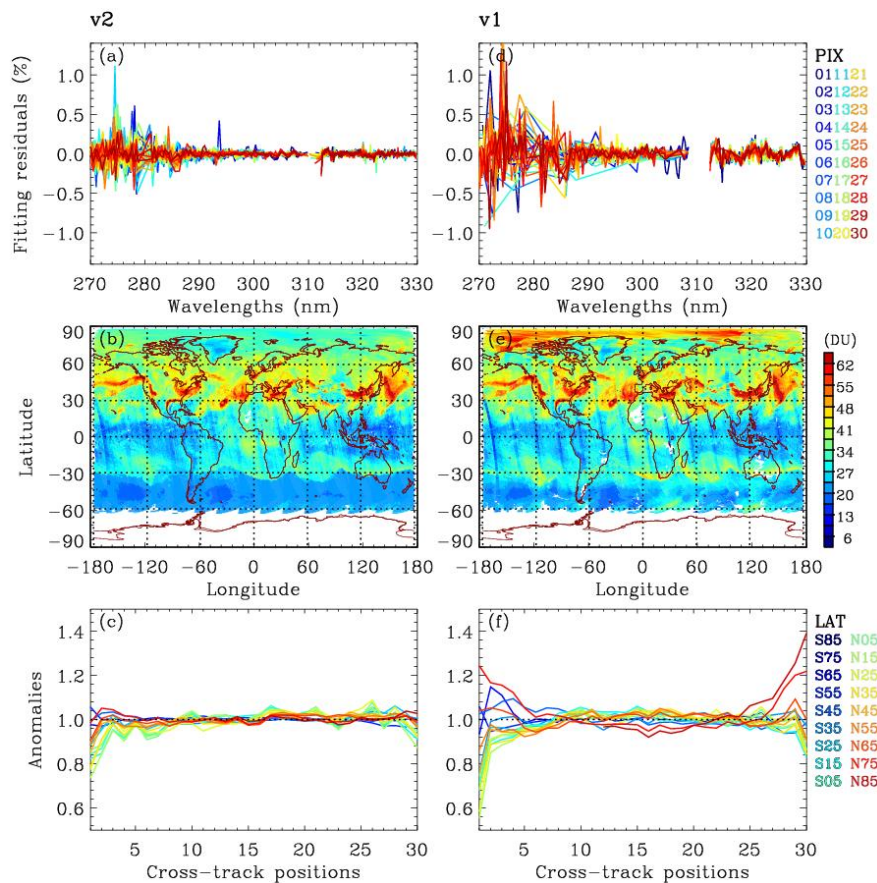
602 3σ are dropped in estimating the comparison statistics. The comparison statistics of tropospheric column
603 ozone between OMI and ozonesondes are summarized in Table 5 for each station. Overall, the mean
604 biases (MBs) are within ± 3 DU (5-10%) with standard deviations (SDs) of 5.5 DU (15%) and
605 correlation coefficients of 0.81-0.85, for the updated product. These comparison statistics represent
606 improvements over those derived for the existing product.

607 Figure 13 shows comparisons of ozone profiles between OMI and ozonesonde during the pre and
608 post Row Anomaly (RA) periods, respectively. The pre-RA period is set to be from the beginning of the
609 mission through 2008 when the row anomaly affects the data in a few rows ~~the row anomalies were~~
610 ~~relatively not serious~~ and the post-RA period is after that. Both v1 and v2 ~~retrievals~~ profiles are
611 positively biased relative to ozonesonde measurements. The ~~mean biases (MBs)~~ of profile differences
612 are less than 20 % over the layers when OMPROFOZ v2 profiles are compared during the pre-RA
613 period. On the other hand, MBs of OMPROFOZ v1 are largely skewed by ~ 45 % in the tropopause
614 region. The comparison also confirms significant improvements of OMPROFOZ v2 retrievals, with the
615 reduction of ~~standard deviations (SDs)~~ by ~ 40 % around the tropopause. These improvements are
616 achieved mainly due to implementing TB ozone profile climatology which could better represent the
617 profile shape in the UTLS as mentioned in Section 3.1. Comparison statistics between OMPROFOZ v2
618 and ozonesondes profiles are generally consistent before and after the RA occurrence in spite of the
619 inconsistent sampling resulting from the occurrence of RA so that only about half of the OMI
620 measurements remain valid, mostly on the west of nadir during the post-RA period. However,
621 OMPROFOZ v1 profiles are shown to be much more affected by temporal changes of OMI instrumental
622 stability, especially in the lower atmosphere.

623 The rest of this section is concentrated on assessing the consistency of tropospheric ozone retrieval
624 quality with respect to temporal changes. For this comparison, tropospheric ozone columns (TCOs) are
625 integrated over the troposphere between 200 hPa and 900 hPa from ozone profiles to avoid the impact
626 of different meteorological inputs used in ~~V1-v1~~ and ~~V2-v2~~ retrievals. In order to check the seasonal
627 changes of retrieval quality, comparison statistics of tropospheric ozone between OMI and ozonesondes
628 are derived for each month during the pre-RA period. The seasonal changes of retrieval quality could
629 be mainly related to the solar zenith angle dependency of OMI measurement sensitivity to the lower
630 tropospheric ozone, which also causes the inconsistency of retrieval quality between lower and higher
631 latitudes. As shown in Figure 14.a, monthly biases of OMI TCO are minimized below ~ 2 DU from
632 June to October when the solar zenith angles are relatively small, commonly for OMPROFOZ v1 and
633 v2. However, the mean biases of OMPROFOZ v1 increase up to ~ 6 -9 DU during January-March, while
634 OMPROFOZ v2 show the moderate change of monthly biases from winter to summer, with the smaller

635 SDs of TCO differences by $\sim 3\text{--}4$ DU during December-March (Fig. 14.b).

636 In order to check the long-term stability, TCO differences are averaged into four seasons for each
 637 year from 2005 to 2020 in Figures 14.c and d. The existence of a long-term drift is clear with MBs of
 638 OMPROFOZ v1 TCO decreasing from $\sim 4.35\text{DU}$ before 2008 to ~ 0.05 DU after 2015. This temporal
 639 drift is largely corrected in OMPROFOZ v2 retrievals and the standard deviations of TCO differences
 640 are reduced generally over the entire period. In addition, OMPROFOZ v1 shows more spikes in both
 641 MBs and SDs than OMPROFOZ v2, especially during the period of 2011 to 2015 when the RA
 642 dynamically expands. Those spikes could be attributed to row anomaly-contaminated retrievals
 643 unscreened with the ~~KNMI-based~~ row anomaly flags taken from OMI collection 3 L1b product (used
 644 in v1). The related improvements in OMPROFOZ v2 retrievals are contributed by applying the stricter
 645 flags taken from OMUANC product, which is considered to be less strict than TOMS-based row
 646 anomaly flags (used in v2).

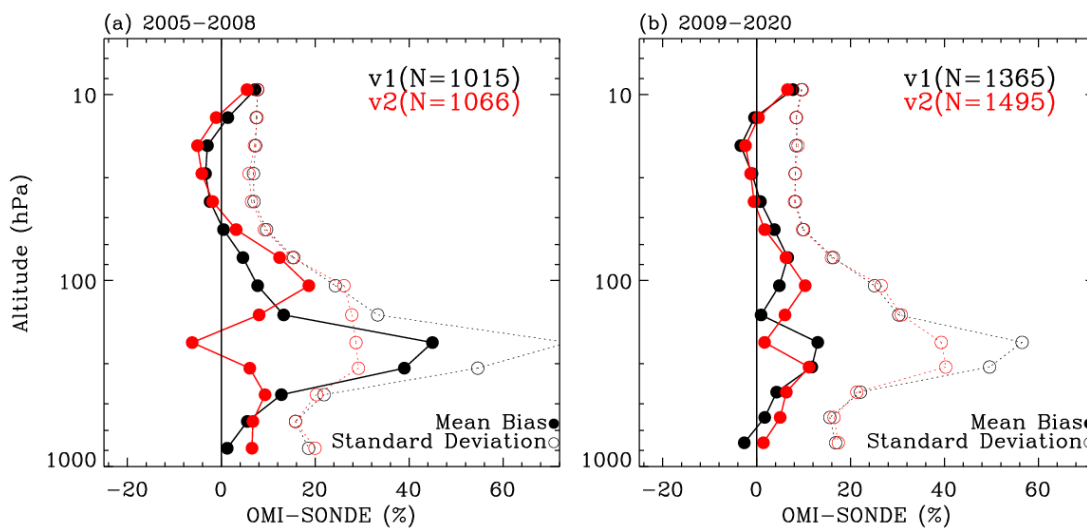


647

648 **Figure 12.** Same as Figure 8, but for V2 (OMI collection 4 product with the final v2 algorithm) and V1 (OMI
 649 collection 3 with the v1 algorithm).

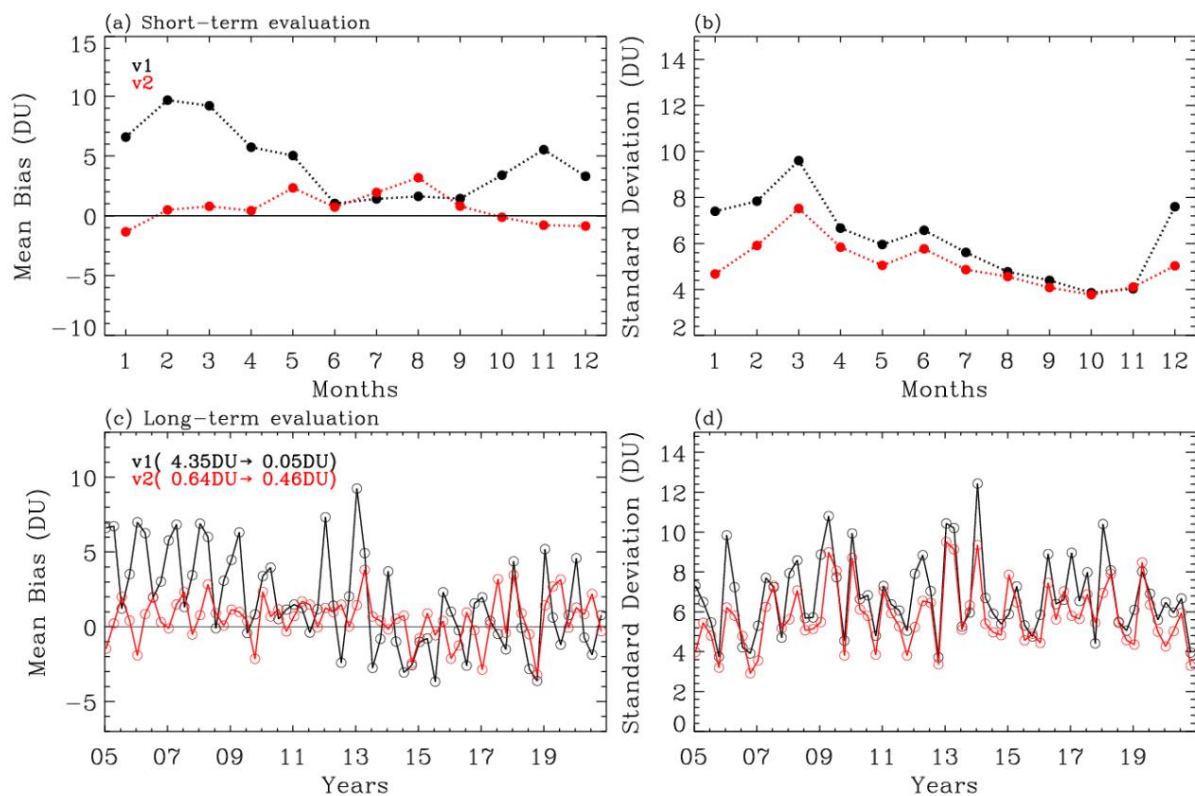
650

651
652
653
654
655
656



657

658 **Figure 13.** Comparisons of ozone profiles between OMI and ozonesonde during (a) pre-row anomaly
659 and (b) post-row anomaly periods, respectively. OMI retrievals are qualified with RMSE < 3, RMS <
660 2%, and cloud fraction less than 0.6. The number of coincident pairs (N) is given in legend.
661



662

663 **Figure 14.** (a) Monthly mean and (b) corresponding standard deviations in differences of tropospheric column
 664 ozone (TCO, 200-900 hPa) between OMI and ozonesondes during the period of 2005 to 2008. (c,d) is same as
 665 (a,b), but for seasonal differences of TCO from 2005 to 2020. The legend of Fig. c represents the overall mean for
 666 the period of 2005-2008 and 2015-2020, respectively.
 667

668 5.8. Summary and Conclusion

669

670 The Smithsonian Astrophysical Observatory (SAO) ozone profile retrieval algorithm has been run
 671 in NASA's Science Investigator-led Processing System (SIPS) to create the Ozone Monitoring
 672 Instrument (OMI) ozone profile (OMPROFOZ) research product, which has not been updated since its
 673 initial data ~~Since the first data~~-release. In this paper, we introduce algorithmic updates for reprocessing
 674 the OMPROFOZ product to enhance, the efforts to improve the retrieval accuracy and to ensure long-
 675 term consistency. ~~of OMI ozone profile retrievals have continued externally. In this paper, the second~~
 676 ~~version of OMPROFOZ research product is introduced, which~~ This second version will be released at
 677 GES-DISC while the first version will remain ~~continue to be~~-archived at AVDC. One of the major
 678 changes is to switch the L1b data from collection 3 to collection 4, for both radiance and irradiance as
 679 well as the accompanying auxiliary datasets. We also changed several geophysical and spectroscopic
 680 inputs including meteorological data, ozone profile climatology, high-resolution solar reference
 681 spectrum, and ozone absorption cross-section dataset. Implementations of forward model calculations

682 and measurements calibrations are improved. The v2 forward model employs a faster principal
683 component analysis (PCA)-based VLIDORT model, along with the LUT-based correction which speeds
684 up the online radiative transfer model calculation while corrections to the approximation produce
685 improved accuracy. The resulting speed-up allows OMI native measurements to be processed for
686 OMPROFOZ v2, with data resolution of $48 \times 26 \text{ km}^2$ at nadir. Note that to meet the computational cost,
687 the previous data were processed after coadding OMI measurements at the spatial resolution of 48×52
688 km^2 . To better represent the shape of OMI slit functions, the slit width and shape factor are
689 parameterized from OMI irradiances, assuming a super Gaussian, instead of a normal Gaussian.
690 Moreover, the effects of slit function differences between radiance and irradiance on ozone retrievals
691 are accounted for as pseudo absorbers in the iterative fit process. The OMI irradiance measurements are
692 included via a monthly average instead of a 3-year climatological mean to cancel out ~~the degradation~~
693 ~~temporally varying calibration parameters commonly existing in~~ ~~offset between~~ radiance and irradiance
694 measurements. The empirical soft calibration spectra are re-derived annually to be consistent with the
695 updated implementations to remove the systematic differences between measured and simulated
696 radiances. “Common mode” correction spectra are derived from remaining residual spectra after soft
697 calibration with the dependency on solar zenith angle. The common mode is included as a pseudo
698 absorber in the iterative fit process, which helps to smooth out the discrepancies of ozone retrieval
699 accuracy between lower and higher solar zenith angles and between nadir and off-nadir pixels.

700 ~~In order to~~ To verify improvements of OMPROFOZ ~~data~~ data quality, both v1 and v2 ozone profiles
701 are ~~evaluated~~ ~~evaluated~~ against ozonesonde measurements ~~taken~~ ~~collected from three stations over from~~
702 central Europe ~~during the period of 2005 to 2020~~. Overall, ~~the consistency of the tropospheric columns~~
703 ~~between OMI and ozonesonde is improved by 0.1-0.15 in correlation coefficients and by 3-6 % in~~
704 ~~standard deviations of individual differences (Tab. 5)~~. It is clearly shown that ozone profile retrievals
705 are greatly improved in the troposphere, especially around the tropopause, with the reduction of mean
706 biases by $\sim 25 \%$ during the pre-RA season (Fig. 13). The standard deviations of mean biases are also
707 improved by $\sim 40 \%$ and $\sim 20 \%$ before and after the RA occurrence. The comparison with ozonesondes
708 also confirms that the temporal consistency of tropospheric ozone quality is improved (Fig. 14). The
709 seasonal change of data quality from summer to winter is predominant in OMI tropospheric ozone with
710 ~~the v1 data~~ processing. However, OMPROFOZ v2 data quality shows much better consistency, with
711 the seasonal changes of retrieval biases within $\sim 2\text{-}3 \text{ DU}$. Above all, we validate that the OMI long-term
712 degradation is better accounted for in ~~OMPROFOZ v2~~ ~~the v2 data~~ processing, along with switching
713 OMI L1b data from collection 3 to collection 4 and updating implementation details. In OMPROFOZ
714 v1, mean biases of tropospheric ozone relative to ozonesonde shows a drift in errors from 4.35 DU to
715 0.05 DU before and after the RA occurrence, which are greatly reduced to within $\pm 0.5 \text{ DU}$ for both

716 periods in OMPROFOZ v2.

717 This new algorithm has been delivered to the NASA OMI SIPS for operational processing and the
718 reprocessing of the entire mission is in progress. The OMPROFOZ v2 product will be distributed via
719 the NASA GES DISC [in 2024](#). [In the follow-up paper to this work, the reprocessed OMI collection 4](#)
720 [ozone profile dataset will be thoroughly evaluated against a comprehensive dataset of ozonesonde](#)
721 [soundings and MLS stratospheric ozone profiles for establishing geophysical validation results and for](#)
722 [assuring the long-term consistency of OMI ozone profile product data quality](#).

723

724 **Author Contributions** J.B and X.L designed the research. X.L developed the OMPROFOZ v1
725 and J.B updated it to OMPROFOZ v2. K.Y contributed to improving the forward model simulations
726 and transferring codes into SIPS; G.G.A and E.O.S developed the reading modules for OMI collection
727 4 products; K.C advised the update to solar reference spectrum; C.H.K provided financial support to
728 make this study continue. J.B and X.L conducted the research and wrote the paper; all authors
729 contributed to the analysis and writing.

730

731 **Competing interests.** The authors have no competing interests

732 **Acknowledgement**

733 Both calculations and simulations are done on the Smithsonian Institution High-Performance Cluster
734 (SI/HPC) (<https://doi.org/10.25572/SIHPC>). We acknowledge the WOUDC for providing ozonesonde
735 data, OMI science team for providing OMI collection 3 and OMI collection 4 products. We would like
736 to thank David Haffner and Zachary Fasnacht for providing useful comments regarding OMI collection
737 4 products.

738

739

740 **Data Availability**

741 ~~All~~ OMI datasets are available at <https://disc.gsfc.nasa.gov/> (last access: ~~21~~ [21 July–December](#)
742 [2023](#)), including [OML1BIRR \(Kleipool, 2021a\)](#), [OML1BRUG \(Kleipool, 2021b\)](#),
743 [OMCLDO2 \(Veefkind, 2012\)](#), [OMUFPMET \(Joiner, 2023a\)](#), [OMUFPSLV \(Joiner, 2023b\)](#),
744 [OMUANC \(Joiner, 2023c\)](#), [OMLER \(Kleipool, 2010\)](#), and [OMTO3 \(Bhartia, 2012\)](#).—The ozonesonde
745 data used to validate our ozone profile retrievals were obtained through the WOUDC. The WOUDC
746 dataset is available at <https://woudc.org/data/products/ozonesonde/> (last access: ~~21~~ [21 December 2023](#)
747 [July 2023](#)).

748

749 **Financial support.** This research has been supported by NASA Aura science team program (grant
750 no. NNX17AI82G and 80NSSC21K0177) and Basic Science Research Program through the National
751 Research Foundation of Korea (NRF) funded by the Ministry of Education (grant no.
752 2020R1A6A1A03044834 and 2021R1A2C1004984).

753

754 **References**

755 AURA-OMI-KNMI-L01B-0005-SD, 2021. Input output data specification for the collection 4 L01b data processing of the
756 Ozone Monitoring Instrument.

757 Bak, J., Baek, K.H., Kim, J.H., Liu, X., Kim, J., Chance, K., 2019a. Cross-evaluation of GEMS tropospheric ozone retrieval
758 performance using OMI data and the use of an ozonesonde dataset over East Asia for validation. Atmos. Meas. Tech.

759 12, 5201–5215. <https://doi.org/10.5194/amt-12-5201-2019>

760 Bak, J., Coddington, O., Liu, X., Chance, K., Lee, H.J., Jeon, W., Kim, J.H., Kim, C.H., 2022. Impact of using a new high-
761 resolution solar reference spectrum on OMI ozone profile retrievals. *Remote Sens.* 14, 1–12.
762 <https://doi.org/10.3390/rs14010037>

763 Bak, J., Liu, X., Birk, M., Wagner, G., Gordon, I.E., Chance, K., 2020. Impact of using a new ultraviolet ozone absorption
764 cross-section dataset on OMI ozone profile retrievals. *Atmos. Meas. Tech.* 13, 5845–5854.
765 <https://doi.org/10.5194/amt-13-5845-2020>

766 Bak, J., Liu, X., Kim, J.-H., Haffner, D.P., Chance, K., Yang, K., Sun, K., 2017. Characterization and correction of OMPS
767 nadir mapper measurements for ozone profile retrievals. *Atmos. Meas. Tech.* 10, 4373–4388.
768 <https://doi.org/10.5194/amt-10-4373-2017>

769 Bak, J., Liu, X., Spurr, R., Yang, K., Nowlan, C.R., Miller, C.C., Abad, G.G., Chance, K., 2021. Radiative transfer
770 acceleration based on the principal component analysis and lookup table of corrections: optimization and application
771 to UV ozone profile retrievals. *Atmos. Meas. Tech.* 14, 2659–2672. <https://doi.org/10.5194/amt-14-2659-2021>

772 Bak, J., Liu, X., Sun, K., Chance, K., Kim, J.-H., 2019b. Linearization of the effect of slit function changes for improving
773 Ozone Monitoring Instrument ozone profile retrievals. *Atmos. Meas. Tech.* 12, 3777–3788.
774 <https://doi.org/10.5194/amt-12-3777-2019>

775 Bak, J., Liu, X., Wei, J.C., Pan, L.L., Chance, K., Kim, J.H., 2013. Improvement of omi ozone profile retrievals in the upper
776 troposphere and lower stratosphere by the use of a tropopause-based ozone profile climatology. *Atmos. Meas. Tech.*
777 6, 2239–2254. <https://doi.org/10.5194/amt-6-2239-2013>

778 Cai, Z., Liu, Y., Liu, X., Chance, K., Nowlan, C.R., Lang, R., Munro, R., Suleiman, R., 2012. Characterization and
779 correction of global ozone monitoring experiment 2 ultraviolet measurements and application to ozone profile
780 retrievals. *J. Geophys. Res. Atmos.* 117, 1–16. <https://doi.org/10.1029/2011JD017096>

781 Chance, K., Kurucz, R.L., 2010. An improved high-resolution solar reference spectrum for earth’s atmosphere
782 measurements in the ultraviolet, visible, and near infrared. *J. Quant. Spectrosc. Radiat. Transf.* 111, 1289–1295.
783 <https://doi.org/10.1016/j.jqsrt.2010.01.036>

784 Coddington, O.M., Richard, E.C., Harber, D., Pilewskie, P., Woods, T.N., Chance, K., Liu, X., Sun, K., 2021. The TSIS-1
785 Hybrid Solar Reference Spectrum. *Geophys. Res. Lett.* 1–10. <https://doi.org/10.1029/2020gl091709>

786 Gaudel, A., Cooper, O.R., Ancellet, G., Barret, B., Boynard, A., Burrows, J.P., Clerbaux, C., Coheur, P.-F., Cuesta, J.,
787 Cuevas, E., Doniki, S., Dufour, G., Ebojje, F., Foret, G., Garcia, O., Granados-Muñoz, M.J., Hannigan, J.W., Hase, F.,
788 Hassler, B., Huang, G., Hurtmans, D., Jaffe, D., Jones, N., Kalabokas, P., Kerridge, B., Kulawik, S., Latter, B.,
789 Leblanc, T., Le Flochmoën, E., Lin, W., Liu, J., Liu, X., Mahieu, E., McClure-Begley, A., Neu, J.L., Osman, M.,
790 Palm, M., Petetin, H., Petropavlovskikh, I., Querel, R., Raupoe, N., Rozanov, A., Schultz, M.G., Schwab, J., Siddans,
791 R., Smale, D., Steinbacher, M., Tanimoto, H., Tarasick, D.W., Thouret, V., Thompson, A.M., Trickl, T.,
792 Weatherhead, E., Wespes, C., Worden, H.M., Vigouroux, C., Xu, X., Zeng, G., Ziemke, J., 2018. Tropospheric Ozone
793 Assessment Report: Present-day distribution and trends of tropospheric ozone relevant to climate and global
794 atmospheric chemistry model evaluation. *Elem. Sci. Anthr.* 6, 39. <https://doi.org/10.1525/elementa.291>

795 Hayashida, S., Liu, X., Ono, A., Yang, K., Chance, K., 2015. Observation of ozone enhancement in the lower troposphere
796 over East Asia from a space-borne ultraviolet spectrometer. *Atmos. Chem. Phys.* 15, 9865–9881.
797 <https://doi.org/10.5194/acp-15-9865-2015>

798 Hu, L., Jacob, D.J., Liu, X., Zhang, Y., Zhang, L., Kim, P.S., Sulprizio, M.P., Yantosca, R.M., 2017. Global budget of
799 tropospheric ozone: Evaluating recent model advances with satellite (OMI), aircraft (IAGOS), and ozonesonde
800 observations. *Atmos. Environ.* 167, 323–334. <https://doi.org/10.1016/j.atmosenv.2017.08.036>

801 Huang, G., Liu, X., Chance, K., Yang, K., Bhartia, P.K., Cai, Z., Allaart, M., Ancellet, G., Calpini, B., Coetsee, G.J.R.,
802 Cuevas-Agulló, E., Cupeiro, M., De Backer, H., Dubey, M.K., Fuelberg, H.E., Fujiwara, M., Godin-Beekmann, S.,
803 Hall, T.J., Johnson, B., Joseph, E., Kivi, R., Kois, B., Komala, N., König-Langlo, G., Laneve, G., Leblanc, T.,
804 Marchand, M., Minschwaner, K.R., Morris, G., Newchurch, M.J., Ogino, S.-Y., Ohkawara, N., Piders, A.J.M., Posny,
805 F., Querel, R., Scheele, R., Schmidlin, F.J., Schnell, R.C., Schrems, O., Selkirk, H., Shiotani, M., Skrivánková, P.,
806 Stübi, R., Taha, G., Tarasick, D.W., Thompson, A.M., Thouret, V., Tully, M.B., Van Malderen, R., Vömel, H., von
807 der Gathen, P., Witte, J.C., Yela, M., 2017. Validation of 10-year SAO OMI Ozone Profile (PROFOZ) product using
808 ozonesonde observations. *Atmos. Meas. Tech.* 10, 2455–2475. <https://doi.org/10.5194/amt-10-2455-2017>

809 Huang, G., Liu, X., Chance, K., Yang, K., Cai, Z., 2018. Validation of 10-year SAO OMI ozone profile (PROFOZ) product
810 using Aura MLS measurements. *Atmos. Meas. Tech.* 11, 17–32. <https://doi.org/10.5194/amt-11-17-2018>

- 811 Kleipool, Q., Rozemeijer, N., van Hoek, M., Leloux, J., Loots, E., Ludewig, A., van der Plas, E., Adrichem, D., Harel, R.,
812 Spronk, S., ter Linden, M., Jaross, G., Haffner, D., Veeffkind, P., Levelt, P.F., 2022. Ozone Monitoring Instrument
813 (OMI) collection 4: establishing a 17-year-long series of detrended level-1b data. *Atmos. Meas. Tech.* 15, 3527–3553.
814 <https://doi.org/10.5194/amt-15-3527-2022>
- 815 Kuang, S., Newchurch, M.J., Johnson, M.S., Wang, L., Burris, J., Pierce, R.B., Eloranta, E.W., Pollack, I.B., Graus, M., de
816 Gouw, J., Warneke, C., Ryerson, T.B., Markovic, M.Z., Holloway, J.S., Pour-Biazar, A., Huang, G., Liu, X., Feng,
817 N., 2017. Summertime tropospheric ozone enhancement associated with a cold front passage due to stratosphere-to-
818 troposphere transport and biomass burning: Simultaneous ground-based lidar and airborne measurements. *J. Geophys.*
819 *Res. Atmos.* 122, 1293–1311. <https://doi.org/https://doi.org/10.1002/2016JD026078>
- 820 Liu, C., Liu, X., Chance, K., 2013. The impact of using different ozone cross sections on ozone profile retrievals from OMI
821 UV measurements. *J. Quant. Spectrosc. Radiat. Transf.* 130, 365–372. <https://doi.org/10.1016/j.jqsrt.2013.06.006>
- 822 Liu, X., Bhartia, P.K., Chance, K., Spurr, R.J.D., Kurosu, T.P., 2010. Ozone profile retrievals from the Ozone Monitoring
823 Instrument. *Atmos. Chem. Phys.* 10, 2521–2537. <https://doi.org/10.5194/acp-10-2521-2010>
- 824 Liu, X., Chance, K., Sioris, C.E., Kurosu, T.P., 2007. Impact of using different ozone cross sections on ozone profile
825 retrievals from Global Ozone Monitoring Experiment (GOME) ultraviolet measurements. *Atmos. Chem. Phys.* 7,
826 3571–3578. <https://doi.org/10.5194/acp-7-3571-2007>
- 827 Liu, X., Chance, K., Sioris, C.E., Spurr, R.J.D., Kurosu, T.P., Martin, R. V., Newchurch, M.J., 2005. Ozone profile and
828 tropospheric ozone retrievals from the Global Ozone Monitoring Experiment: Algorithm description and validation. *J.*
829 *Geophys. Res.* 110, D20307. <https://doi.org/10.1029/2005JD006240>
- 830 Lu, X., Zhang, L., Liu, X., Gao, M., Zhao, Y., Shao, J., 2018. Lower tropospheric ozone over India and its linkage to the
831 South Asian monsoon. *Atmos. Chem. Phys.* 18, 3101–3118. <https://doi.org/10.5194/acp-18-3101-2018>
- 832 Luo, J., Pan, L.L., Honomichl, S.B., Bergman, J.W., Randel, W.J., Francis, G., Clerbaux, C., George, M., Liu, X., Tian, W.,
833 2018. Space-time variability in UTLS chemical distribution in the Asian summer monsoon viewed by limb and nadir
834 satellite sensors. *Atmos. Chem. Phys.* 18, 12511–12530. <https://doi.org/10.5194/acp-18-12511-2018>
- 835 McPeters, R.D., Labow, G.J., 2012. Climatology 2011: An MLS and sonde derived ozone climatology for satellite retrieval
836 algorithms. *J. Geophys. Res. Atmos.* 117. <https://doi.org/https://doi.org/10.1029/2011JD017006>
- 837 McPeters, R.D., Labow, G.J., Logan, J.A., 2007. Ozone climatological profiles for satellite retrieval algorithms. *J. Geophys.*
838 *Res.* 112, D05308. <https://doi.org/10.1029/2005JD006823>
- 839 Munro, R., Siddans, R., Reburn, W.J., Kerridge, B.J., 1998. Direct measurement of tropospheric ozone distributions from
840 space. *Nature* 392, 168–171. <https://doi.org/10.1038/32392>
- 841 Orphal, J., Staehelin, J., Tamminen, J., Braathen, G., De Backer, M.-R., Bais, A., Balis, D., Barbe, A., Bhartia, P.K., Birk,
842 M., Burkholder, J.B., Chance, K., von Clarmann, T., Cox, A., Degenstein, D., Evans, R., Flaud, J.-M., Flittner, D.,
843 Godin-Beekmann, S., Gorschelev, V., Gratien, A., Hare, E., Janssen, C., Kyrölä, E., McElroy, T., McPeters, R., Pastel,
844 M., Petersen, M., Petropavlovskikh, I., Picquet-Varrault, B., Pitts, M., Labow, G., Rotger-Languereau, M., Leblanc,
845 T., Lerot, C., Liu, X., Moussay, P., Redondas, A., Van Roozendaal, M., Sander, S.P., Schneider, M., Serdyuchenko,
846 A., Veeffkind, P., Viallon, J., Viatte, C., Wagner, G., Weber, M., Wielgosz, R.I., Zehner, C., 2016. Absorption cross-
847 sections of ozone in the ultraviolet and visible spectral regions: Status report 2015. *J. Mol. Spectrosc.* 327, 105–121.
848 <https://doi.org/https://doi.org/10.1016/j.jms.2016.07.007>
- 849 Schenkeveld, V.M.E., Jaross, G., Marchenko, S., Haffner, D., Kleipool, Q.L., Rozemeijer, N.C., Veeffkind, J.P., Levelt, P.F.,
850 2017. In-flight performance of the Ozone Monitoring Instrument. *Atmos. Meas. Tech.* 10, 1957–1986.
851 <https://doi.org/10.5194/amt-10-1957-2017>
- 852 Sun, K., Liu, X., Huang, G., González Abad, G., Cai, Z., Chance, K., Yang, K., 2017. Deriving the slit functions from OMI
853 solar observations and its implications for ozone-profile retrieval. *Atmos. Meas. Tech.* 10, 3677–3695.
854 <https://doi.org/10.5194/amt-10-3677-2017>
- 855 Walker, T.W., Martin, R. V., Van Donkelaar, A., Leaitch, W.R., MacDonald, A.M., Anlauf, K.G., Cohen, R.C., Bertram,
856 T.H., Huey, L.G., Avery, M.A., Weinheimer, A.J., Flocke, F.M., Tarasick, D.W., Thompson, A.M., Streets, D.G., Liu,
857 X., 2010. Trans-pacific transport of reactive nitrogen and ozone to Canada during spring. *Atmos. Chem. Phys.* 10,
858 8353–8372. <https://doi.org/10.5194/acp-10-8353-2010>
- 859 Wei, J., Li, Z., Li, K., Dickerson, R.R., Pinker, R.T., Wang, J., Liu, X., Sun, L., Xue, W., Cribb, M., 2022. Full-coverage
860 mapping and spatiotemporal variations of ground-level ozone (O₃) pollution from 2013 to 2020 across China. *Remote*
861 *Sens. Environ.* 270. <https://doi.org/10.1016/j.rse.2021.112775>

862 Zhang, L., Jacob, D.J., Liu, X., Logan, J.A., Chance, K., Eldering, A., Bojkov, B.R., 2010. Intercomparison methods for
863 satellite measurements of atmospheric composition: Application to tropospheric ozone from TES and OMI. *Atmos.*
864 *Chem. Phys.* 10, 4725–4739. <https://doi.org/10.5194/acp-10-4725-2010>

865 Zhao, F., Liu, C., Cai, Z., Liu, X., Bak, J., Kim, J., Hu, Q., Xia, C., Zhang, C., Sun, Y., Wang, W., Liu, J., 2021. Ozone
866 profile retrievals from TROPOMI: Implication for the variation of tropospheric ozone during the outbreak of COVID-
867 19 in China. *Sci. Total Environ.* 764, 142886. <https://doi.org/10.1016/j.scitotenv.2020.142886>

868 Ziemke, J.R., Olsen, M.A., Witte, J.C., Douglass, A.R., Strahan, S.E., Wargan, K., Liu, X., Schoeberl, M.R., Yang, K.,
869 Kaplan, T.B., Pawson, S., Duncan, B.N., Newman, P.A., Bhartia, P.K., Heney, M.K., 2014. Assessment and
870 applications of NASA ozone data products derived from Aura OMI/MLS satellite measurements in context of the
871 GMI chemical transport model. *J. Geophys. Res. Atmos.* 119, 5671–5699.
872 <https://doi.org/https://doi.org/10.1002/2013JD020914>

873 Zoogman, P., Liu, X., Suleiman, R.M., Pennington, W.F., Flittner, D.E., Al-Saadi, J.A., Hilton, B.B., Nicks, D.K.,
874 Newchurch, M.J., Carr, J.L., Janz, S.J., Andraschko, M.R., Arola, A., Baker, B.D., Canova, B.P., Chan Miller, C.,
875 Cohen, R.C., Davis, J.E., Dussault, M.E., Edwards, D.P., Fishman, J., Ghulam, A., González Abad, G., Grutter, M.,
876 Herman, J.R., Houck, J., Jacob, D.J., Joiner, J., Kerridge, B.J., Kim, J., Krotkov, N.A., Lamsal, L., Li, C., Lindfors,
877 A., Martin, R. V., McElroy, C.T., McLinden, C., Natraj, V., Neil, D.O., Nowlan, C.R., O’Sullivan, E.J., Palmer, P.I.,
878 Pierce, R.B., Pippin, M.R., Saiz-Lopez, A., Spurr, R.J.D., Szykman, J.J., Torres, O., Veefkind, J.P., Veihelmann, B.,
879 Wang, H., Wang, J., Chance, K., 2017. Tropospheric emissions: Monitoring of pollution (TEMPO). *J. Quant.*
880 *Spectrosc. Radiat. Transf.* 186, 17–39. <https://doi.org/10.1016/j.jqsrt.2016.05.008>

881 [Kroon, M., de Haan, J. F., Veefkind, J. P., Froidevaux, L., Wang, R., Kivi, R., and Hakkarainen, J. J. \(2011\). Validation of](#)
882 [operational ozone profiles from the Ozone Monitoring Instrument, *J. Geophys. Res.*, 116, D18305,](#)
883 [doi:10.1029/2010JD015100.](#)

884 [Lamsal, L. N., Krotkov, N. A., Vasilkov, A., Marchenko, S., Qin, W., Yang, E.-S., Fasnacht, Z., Joiner, J., Choi, S., Haffner,](#)
885 [D., Swartz, W. H., Fisher, B., and Bucsel, E.: Ozone Monitoring Instrument \(OMI\) Aura nitrogen dioxide standard](#)
886 [product version 4.0 with improved surface and cloud treatments, *Atmos. Meas. Tech.*, 14, 455–479,](#)
887 [<https://doi.org/10.5194/amt-14-455-2021>, 2021.](#)

888 [Wang, H., Gonzalez Abad, G., Liu, X., and Chance, K.: Validation and update of OMI Total Column Water Vapor product,](#)
889 [*Atmos. Chem. Phys.*, 16, 11379–11393, <https://doi.org/10.5194/acp-16-11379-2016>, 2016.](#)

890 Kleipool, Q. (2021a), OMI/Aura Level 1B Averaged Solar Irradiances V004, Greenbelt, MD, USA, Goddard Earth Sciences
891 Data and Information Services Center (GES DISC), Accessed: [2023-07-21], 10.5067/Aura/OMI/DATA1401, 2021a

892 Kleipool, Q. (2021b), OMI/Aura Level 1B UV Global Geolocated Earthshine Radiance V004, Greenbelt, MD, USA, Goddard
893 Earth Sciences Data and Information Services Center (GES DISC), Accessed: [2023-07-
894 21],10.5067/AURA/OMI/DATA1402

895 Joiner, J. (2023,a), GEOS-5 FP-IT 3D Time-Averaged Single-Level Diagnostics Geo-Colocated to OMI/Aura UV2 1-Orbit
896 L2 Swath 13x24km V4, NASA Goddard Space Flight Center, Goddard Earth Sciences Data and Information Services
897 Center (GES DISC), Accessed: [2023-07-21], 10.5067/Aura/OMI/DATA2435

898 Joiner, J. (2023,b), GEOS-5 FP-IT 3D Time-Averaged Model-Layer Assimilated Data Geo-Colocated to OMI/Aura VIS 1-
899 Orbit L2 Swath 13x24km V4, NASA Goddard Space Flight Center, Goddard Earth Sciences Data and Information
900 Services Center (GES DISC), Accessed: [2023-07-21], 10.5067/Aura/OMI/DATA2436

901 Joiner, J. (2023,c), Primary Ancillary Data Geo-Colocated to OMI/Aura UV2 1-Orbit L2 Swath 13x24km V4, NASA Goddard
902 Space Flight Center, Goddard Earth Sciences Data and Information Services Center (GES DISC), Accessed: [2023-07-
903 21], 10.5067/Aura/OMI/DATA2438

904 Veefkind, P (2012), OMI/Aura Cloud Pressure and Fraction (O2-O2 Absorption) Daily L2 Global Gridded 0.25 degree x 0.25
905 degree V3, Greenbelt, MD, USA, Goddard Earth Sciences Data and Information Services Center (GES DISC),
906 Accessed: [2023-07-21], 10.5067/Aura/OMI/DATA2008

907 Kleipool, Q (2010), OMI/Aura Surface Reflectance Climatology L3 Global Gridded 0.5 degree x 0.5 degree V3, Greenbelt,
908 MD, USA, Goddard Earth Sciences Data and Information Services Center (GES DISC), Accessed: [2023-07-
909 21], 10.5067/Aura/OMI/DATA3006

910 Bhartia, P.K (2012), OMI/Aura TOMS-Like Ozone, Aerosol Index, Cloud Radiance Fraction L3 1 day 1 degree x 1 degree
911 V3, NASA Goddard Space Flight Center, Goddard Earth Sciences Data and Information Services Center (GES DISC),
912 Accessed: [2023-07-21], 10.5067/Aura/OMI/DATA3001